Università degli Studi di Padova

DIPARTIMENTO DI FISICA E ASTRONOMIA "GALILEO GALILEI"
Corso di Laurea Magistrale in Astronomia

Tesi di laurea magistrale

Comptonization in strongly magnetized media

Candidato:
Maria Spezzati
Matricola 1149632

Relatore:
Prof. Roberto Turolla

Correlatore:
Dott. Roberto Taverna

Anno Accademico 2017-2018

Contents

Introduction

The study of neutron stars (NSs) allows to investigate properties of matter and processes that occur under extreme conditions. Their strong magnetic fields ($\gtrsim 10^{12}$ G), far higher than the ones achievable in a terrestrial laboratory, make them perfect candidates to test theoretical physics under conditions which in no way can be reached with our instruments.

X-ray pulsars are neutron stars which accrete mass from a companion star. The strong X-ray emission is given by the accretion of matter onto the NS surface which is strongly affected by the NS magnetic field ($B > 10^9$ G): the accreting material from the accretion disk follows the magnetic field lines toward the magnetic poles, forming an accretion column. Inside this structure the material is heated to high temperatures and the opacity is dominated by the scattering between electrons and photons (Basko & Sunyaev 1975). Because of the high B, the X-ray photons are expected to be strongly polarized in two normal modes, the ordinary and the extraordinary mode, defined by the direction of the photon polarization vector with respect to that of the local magnetic field. Scattering cross sections in the presence of strong magnetic fields are quite different for the two modes; in particular, the cross section which involve X-mode photons turns out to be much lower than that for O-mode ones (see Canuto et al. 197; Gnedin & Pavlov, 1974). Photon propagation becomes really angle-dependent adding a further complexity in solving the already complicated integro-differential radiation transport equation which provides the description of the outgoing radiation and NS spectra.

The arrival of future missions, like the NASA IXPE[1] (Imaging X-ray Polarimetry Explorer), with new generation X-ray polarimeters promise to add more information to high energy astrophysical observations through polarimetric measurements. In fact, so far NSs were studied only through the timing and spectroscopic measurements which could not provide a unique and complete description of the geometry of these sources because of the spectral degeneracy: the same spectral characteristics can be linked to different combinations of the parameters of these sources. X-ray polarimetry will be the key to remove this ambiguity because polarization is strongly affected by the magnetic field and so a measure of the degree and the orientation of the polarized radiation would lead to a better description of the NS magnetic field and its geometry as for the accretion columns.

In this thesis we focus on the Compton scattering in presence of a strong magnetic field, which is one of the dominant processes in NS atmospheres and particularly in structures like

[1] https://ixpe.msfc.nasa.gov

accretion columns in X-ray pulsars. Following the previous works by Nagel (1981) and Mészáros (1992), we analyze the differential cross section in the non-relativistic limit for a hot plasma. This quantity is extremely important for the numerical solution of the radiative transfer equation in a scattering-dominated medium beyond two-stream approximation which was used so far. In order to understand the spectral and polarization properties of the radiation emitted from NSs, it is important to produce a valid numerical code which allows to solve consistently the radiative transfer in such a medium within reasonable computational times.

This thesis is organized as follows:

- In chapter 1 we give a general description of neutron stars and in particular of accreting columns;
- In chapter 2 we describe the motion of particles in a strong magnetic field, polarization modes of radiation and their evolution when propagating in a magnetized medium;
- In chapter 3 we describe the radiation transport equation;
- In chapter 4 we introduce the quantum formalism for the magnetic Compton scattering;
- In chapter 5 we perform the analysis of the differential scattering cross section and its numerical integration;
- Chapter 6 contains the conclusions.

Chapter 1

Neutron stars

Neutron stars (NSs) are extreme compact objects that are born in the core-collapse of massive stars ($8 \lesssim M/M_\odot \lesssim 25$), after a supernova (SN) explosion. At the end of the stellar evolution, when all the nuclear fuel is exhausted, the hydrostatic equilibrium no longer holds since the energy produced by the fusion is not enough to counterbalance the gravitational force and so the star collapses. If the core mass is less than the Chandrasekhar mass $M_{Ch} = 1.44 M_\odot$, the degenerate electron gas pressure prevents the star against further contractions and so it becomes a white dwarf (WD). If $M > M_{Ch}$ the degenerate electron gas pressure is not sufficient anymore and the star keeps contracting. At $\rho_d = 4.3 \times 10^{11}$ g cm^{-3}, which is called neutron drip density, free neutrons appear in the interior of the star due to the inverse β processes:

$$p^+ + e^- \rightarrow n^0 + \nu_e \,, \tag{1.1}$$

which counterbalances the neutron decay. Density keeps increasing until the degenerate neutron gas pressure, together with the repulsive part of the strong nuclear force, becomes strong enough to stop the collapse and a NS is formed. If instead the initial stellar mass is larger than about $25 M_\odot$ neither the degenerate neutron gas pressure nor any other mechanism can oppose the gravitational force and so the star keeps collapsing becoming a black hole (BH). Typical values for the NS radius are between $10 - 20$ km and masses between $1 - 2 M_\odot$ so they achieve huge densities, comparable or even higher than for an atomic nucleus ($\rho_n = 10^{14}$ g/cm^3).

The internal structure of a NS can be divided in five regions (Camenzind 2007):

- atmosphere which is just few centimeters thick;
- outer crust (10^6 g cm$^{-3} \leq \rho \leq 4.3 \times 10^{11}$ g cm^{-3}), a solid region made by a Coulomb lattice of heavy nucleons and a gas of relativistic degenerate electrons in equilibrium against the β decay, (this part is very similar to the interior of a WD);
- inner crust (4.3×10^{11} g cm$^{-3} \leq \rho \leq (2 - 2.4) \times 10^{14}$ g cm^{-3}), that consists in a lattice of neutron-rich nucleons with a gas of superfluid neutrons and electrons;
- outer core ($2 - 2.4 \times 10^{14} \leq 6 \times 10^{14}$ g cm^{-3}), mainly composed by superfluid neutrons with some superconductive protons, relativistic electrons and muons;

- inner core ($\rho \gtrsim 6 \times 10^{14}$ g cm^{-3}), the nature of which is not clear yet, can contain hyperons, more massive baryon resonances, $\pi-$ and K- meson condensates and possibly deconfined quarks.

Other two important features of NSs are the short rotational period and the huge magnetic field, both of which can be explained invoking conservation laws during the core collapse. If we assume that the angular momentum is conserved, then $I_f \omega_f = I_i \omega_i$, where I is the inertial momentum, ω is the angular velocity and the star can be assumed as a homogeneous sphere (so that $I = 2/5 MR^2$). Assuming that the mass of the progenitor star before the core collapse and that of the compact object are of the same order of magnitude, we find $\omega_f = \omega_i R_i^2 / R_f^2$. Since the angular velocity and the period P are linked by the relation $\omega = 2\pi/P$ we finally obtain

$$P_f = P_i \left(\frac{R_f}{R_i} \right)^2 . \tag{1.2}$$

Taking for the initial star typical values as $P_i \sim 10^5$ s ~ 1 day and $R_i \sim 10^6$ km and supposing $R_f \sim 10$ km, we obtain a period of $P_f \sim 10^{-5}$ s. NSs with period between $10^{-3} \leq P \leq 10$ s has been observed. Thus NSs are expected to be really fast rotators, especially at the beginning of their life because then the spin decreases as we will see.

As done for the angular momentum, we calculate the NS magnetic field assuming that the magnetic flux is conserved during the collapse:

$$B_f R_f^2 = B_i R_i^2 \Rightarrow B_f = B_i \left(\frac{R_i}{R_f} \right)^2 . \tag{1.3}$$

Using the same values for the radii and considering $B_i = 100$ G we find $B_f \sim 10^{12}$ G. This makes NSs powerful magnets, the strongest discovered until now in the universe . So far NSs with a magnetic field up to 10^{15} G were found.

The magnetic field, together with the rotation of the star, is the responsible for the behavior and the evolution of the NS and in particular for the decrease of the rotation period. Although generally it is not trivial to develop a well-defined model for the magnetic field of NS, we will simplify here and suppose that it is a dipole, so in spherical coordinates it is

$$\boldsymbol{B}_{dip} = \frac{B_p R^3}{r^3} \left(\cos\theta \boldsymbol{e}_r + \frac{\sin\theta}{2} \boldsymbol{e}_\theta \right), \tag{1.4}$$

where B_p is the intensity of the magnetic field at the magnetic poles and r and θ the radial and polar coordinates respectively. The magnetic dipole moment $m = 1/2\, BR^3$ and the rotation axis are in general misaligned, so the magnetic field lines rotate rigidly with the star. A rotating dipole emits radiation whose power is given by the Larmor formula

$$\dot{E} = -\frac{2}{3c^3} \mid \ddot{\boldsymbol{m}} \mid^2 = -\frac{2}{3c^3} \frac{B^2 R^6 \omega^4 \sin^2\alpha}{4} \tag{1.5}$$

where α is the angle between the two vectors $\boldsymbol{\omega}$ and $\boldsymbol{m}$. The minus sign implies that the energy is taken away from the star. This energy is simply the rotational energy $E_{sd} = I\omega^2/2$, so the

loss of rotational energy or spin-down luminosity is

$$\dot{E}_{sd} = I\omega\dot{\omega}. \tag{1.6}$$

This implies that $\dot{\omega}$ is negative, which means that the star is slowing down. The evolution of the rotation period is therefore given by

$$\dot{\omega} = -\frac{B^2 R^6 \omega^3 \sin^2\alpha}{6Ic^3}. \tag{1.7}$$

We can now calculate the spin-down magnetic field at the poles as a function of P and $\dot{P}$ equating 1.5 and 1.6

$$B_{sd} = B_p = \sqrt{\frac{3Ic^3}{4\pi^2 R \sin^2\alpha} P\dot{P}} \simeq 3.2 \times 10^{19}\sqrt{P\dot{P}}\,\mathrm{G}, \tag{1.8}$$

where we have used $R = 10$ km, $M = 1.5M_\odot$, $I = 10^{45}\,\mathrm{g\,cm^2}$ and $\sin^2\alpha = 1$. Integrating eq. 1.7 over time t, it is possible to calculate the characteristic age τ_c of the NS, assuming that the initial angular velocity is far higher than the final one, that B remains constant and that the loss of energy is completely due to the magnetic dipole radiation:

$$\tau_c = \frac{P}{2\dot{P}}. \tag{1.9}$$

From these calculations, P and $\dot{P}$ turn to be two fundamental quantities to characterize NSs, which therefore are usually represented in the $P - \dot{P}$ diagram. As shown in Figure 1.1, different types of NSs (see next section) occupy different regions of the diagram. If the star magnetic field does not change, a NS evolves moving in the diagram to larger period following a line of constant B, like a normal star evolves along a track in the Hertzsprung-Russell diagram.

1.1 Neutron star zoo

Even if theorized in the 30s (Baade & Zwicky 1934), the first observation of a NS took place in 1967 when it was discovered the first radio pulsar (PSRs) (Hewish et al. 1968). Then, with the improvement of high-energy observations in the '90s, other types of NSs were identified and now, altought radio PSRs are the most numerous class, NSs are observed across the entire electromagnetic spectrum.

They are classified according to the position in the $P - \dot{P}$ diagram which is linked to the primary power source for their emission and spin evolution. Rotation-Powered Pulsars (RPPs) derive their energy primarily from the rotation of the star as seen in the previous section. The rotation of neutron stars is responsible for the observation of their pulsed emission at radio and X-ray wavelengths, the pulses being attributed to the passage of a beam of radiation from the magnetic poles of the neutron star across the observer line-of-sight. To account for the observation of radio pulses, the magnetic axis of the star, where the beam of radio emission is

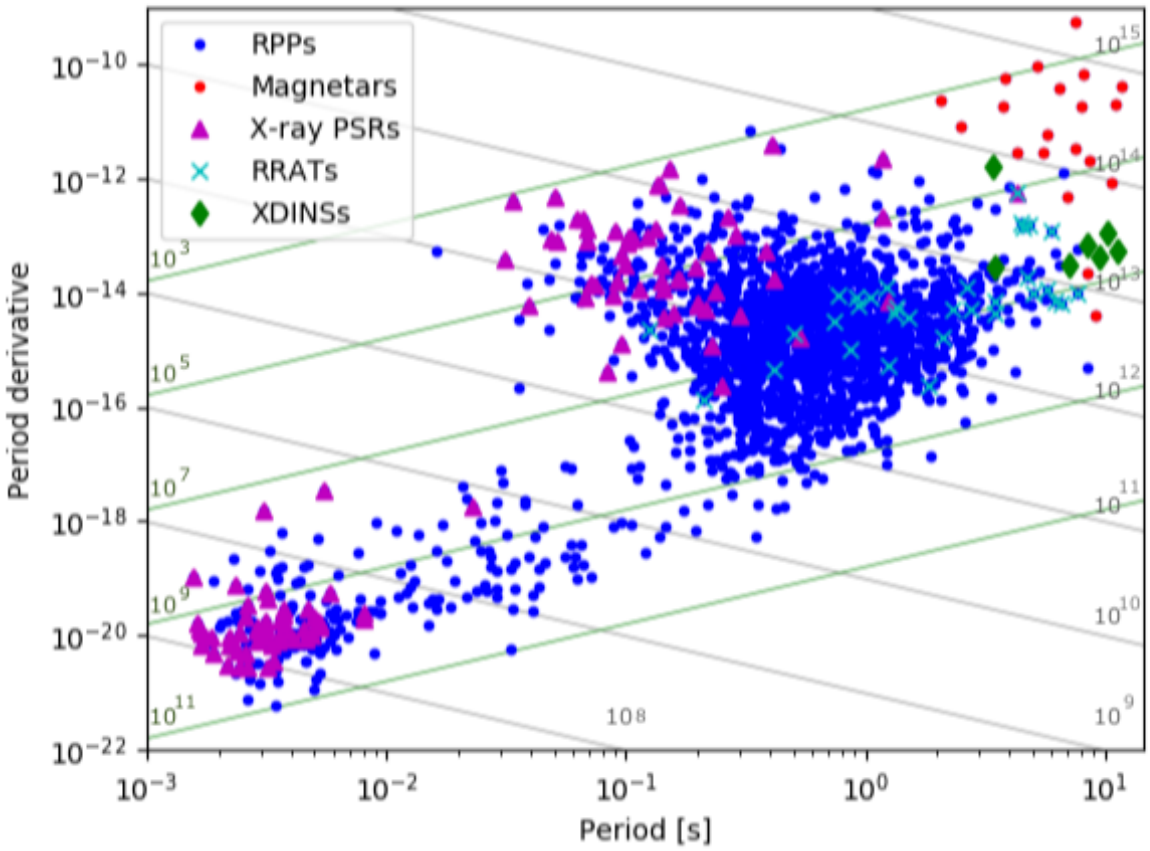

Figure 1.1: $P - \dot{P}$ diagram in logarithmic scale of the presently known NSs of different classes: Rotation-Powered Pulsar (RPPs, blue-filled circles), Magnetars (red-filled circles), Rotating Radio Transients (RRTs, cyan crosses), X-ray Dim Isolated Neutron Stars (XDINSs, green diamonds). X-ray emitting pulsars are highlighted by the purple triangles. (`http://www.atnf.csiro.au/people/pulsar/psrcat/`). Lines of constant B_p (grey) and characteristic age τ_c (green) are superimposed.

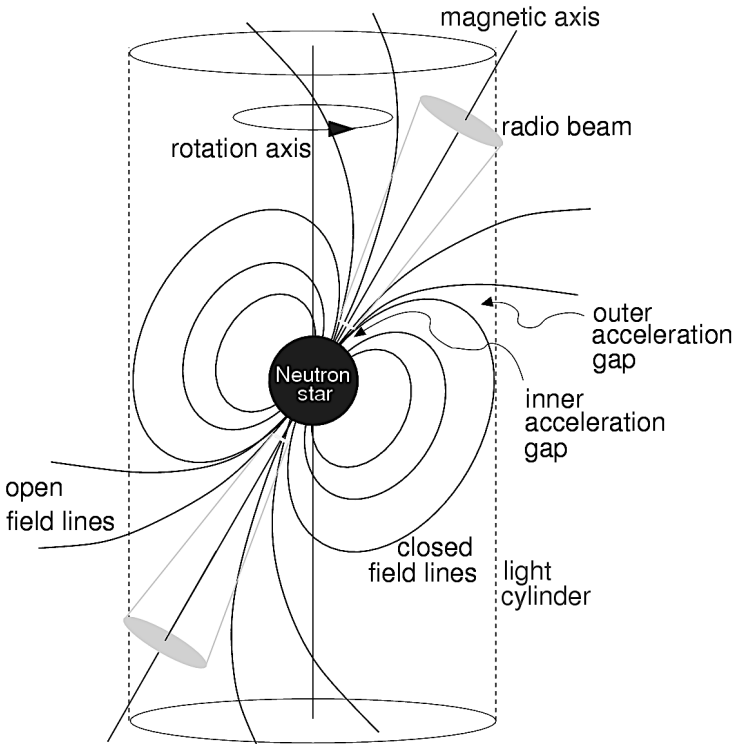

Figure 1.2: Schematic model of a pulsar with the magnetic and rotation axes misaligned (Lorimer & Kramer 2005).

originated, and its rotation axis must be misaligned. There are two main populations of RPPs: ordinary pulsars with $\tau \leq 10^5$ yr and periods in the range $10^{-1} - 1$ s and millisecond pulsars (MSPs) which have rotation periods between $1 - 10$ ms and $\tau \geq 10^8$ yr. Ordinary radio pulsars are thought to have increased their rotation periods at a steady rate from their birth. On the other hand, MSP short periods contrast with their old ages. The leading theory for the origin of millisecond pulsars is that they were born in a binary system and then were spun up or "recycled" by accretion from the companion. For this reason, millisecond pulsars are sometimes called recycled pulsars.

Isolated Neutron Stars (INSs) are NSs whose X-ray emission is not powered by the rotational energy losses. This group includes X-ray dim isolated neutron stars (XDINSs), central compact objects (CCOs), rotating radio transients (RRATs) and magnetars.

Magnetars are characterized by a ultra-strong magnetic fields and by the emission of repeated bursts in the hard-X/soft-gamma-ray. They were initially classified in two different groups, the soft-gamma-ray repeaters (SGRs) and the anomalous X-ray pulsars (AXPs). SGRs were firstly associated with gamma-ray bursts (GRBs) but then the repetition of the burst events excluded this association since GRBs are unique events. AXPs were identified as anomalous pulsars because of their luminosities far higher than $\dot{E}_{sd}$. The leading scenario for which AXPs and SGRs are different manifestations of the same objects, the magnetars (Duncan & Thompson,

1992), is sustained by the great number of properties shared by these two classes. They exhibit long rotation periods, between $2 - 12$ s and period derivatives in the range $10^{-13} - 10^{-11}$ s s^{-1}, leading to characteristic ages between $10^3 - 10^6$ yr and spin-down magnetic fields up to 10^{15} G.

XDINSs, also known as The Magnificent Seven, are seven close-by objects whose emission is peaked in the X-ray (X-ray to optical flux ratio $\approx 10^4 - 10^5$) with luminosities $L_X \approx 10^{30} - 10^{32}$ erg s^{-1}. They present rotational periods $P \approx 3 - 11$ s and quite large period derivatives $\dot{P} \approx 10^{-14} - 10^{-13}$s s^{-1}. These values lead to quite high values for the surface magnetic fields $B_{sd} \approx 10^{13}$ G. Their unusually strong magnetic fields could act as an additional source of heating that would explain their high luminosity. XDINSs are thought to be the evolution of magnetars in which the magnetic field has substantially decayed (Mignani et al. 2008).

CCOs are INSs located at the center of supernova remnants (SNRs). Since there are only few direct measurements of the spin periods, the age of these objects is inferred from that of the SNR (which is approximately 10^4 yr). This indicates that they are young NSs (Halpern & Gotthelf 2010). From the objects for which a measure has been possible, the period derivatives turn out to be of the order of $\dot{P} \approx 10^{-18} - 10^{-16}$ s s^{-1} and this lead to a value of the spin down magnetic field of $B_{sd} \approx 10^{10} - 10^{11}$ G, the lowest ever estimated for INSs.

RRATs are a class of radio-emitting neutron stars recently discovered (McLaughlin et al. 2006). They show sporadic emission of single pulses which last $\approx 2 - 30$ ms. The number of observed RRATs is still very small, only $\sim$100 RRATs[1]. It is not clear yet the reason why RRATs present this irregular emission. It has been suggested that RRATs may be related to magnetars and XDINS (McLaughlin et al. 2006; Lyne et al. 2009) because some of these objects exhibit long periods and higher magnetic fields than normal pulsars ($B_{RRAT} \approx 10^{13}$ G). However, the link between RRATs and other classes of NSs is not yet understood also because they are found really scattered all over the $P - \dot{P}$ diagram.

X-ray Pulsars (XRPs) are magnetized ($B > 10^9$ G) NSs with a companion star that can be a low-mass main sequence star or a massive star like a B-type star. In the first case they form a low-mass X-ray Binary (LMXB) while in the second one a high-mass X-ray Binary (HMXB). Their X-ray emission comes from the accretion of material from the companion star. The magnetic field channels the accreting material towards the magnetic poles, producing what is called an accretion column, where the kinetic energy of the free fall is converted into X-ray thermal emission. Inside the accretion column the opacity is dominated by the scattering between photons and electrons. Being close to the NS surface, this processes are strongly influenced by the NS magnetic field. That is why a better comprehension of the scattering process in a strong medium is needed to explain this kind of structure.

[1]See the 'RRATalog' for details on all known RRATs: http: //astro.phys.wvu.edu/rratalog

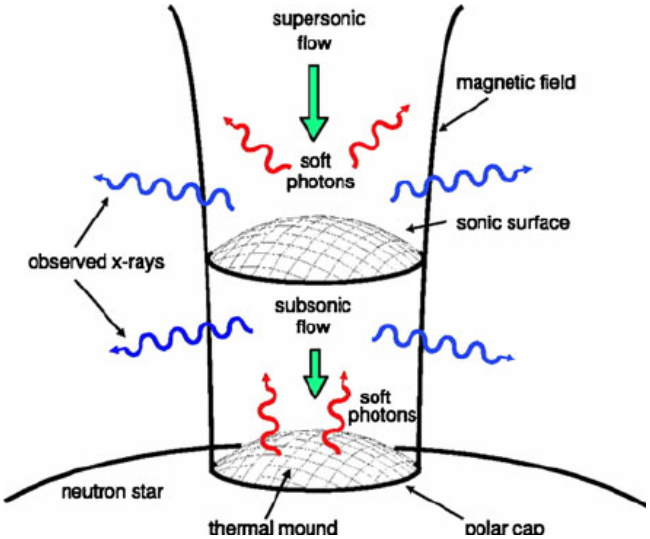

Figure 1.3: Schematic view of the accretion column (Becker & Wolff 2007).

1.2 Accreting columns

The accreting material forms a disk outside the Alfén radius, i.e. the radius R_A at which the stellar magnetic field pressure equals the RAM pressure. At R_A the disk is truncated and from this point the material follows the magnetic field lines and falls freely towards the magnetic poles in a long and narrow funnel, the accretion column. Estimated values for the accretion column radius a, width d and length l are $a \sim 0.1 R_{NS} \simeq 10^5$ cm centered at the magnetic pole, $d \ll a$ around 10^3 cm and $l = 2a$ (Basko & Sunyaev 1975).

In the accretion column matter is slowed down from supersonic to subsonic velocities. We can therefore distinguish two different regions: the free fall region in which matter has a supersonic velocity $v = (2GM/r)^{1/2} \sim 0.65c$ and the shock region in which instead matter velocity is subsonic (Figure 1.3). The first region is the largest one, it extends nearly till the NS surface. The second one is really thin but it is here where gas slows down and a high radiation density is found (Basko & Sunyaev 1976). It is from this second zone that the radiation escapes freely. Basko & Sunyaev (1976) found a critical value for the mass accretion rate and hence the luminosity which separates between two different accreting regimes, the high-rate and the low-rate ones,

$$L_{crit} = \frac{d}{R}\frac{c}{\kappa}\frac{2GM}{R}$$

where M and R are the NS mass and radius, κ the opacity. Normally L_{crit} is comparable to the Eddington luminosity L_{Edd} (Nelson et al. 1993). For $L_X \gtrsim L_{crit}$ the radiation pressure is far higher than the gas pressure and so it dominates the shock. The accreting material is indeed impeded by the emerging radiation, the accretion column becomes opaque along the magnetic field axis so the X-ray photons can escape from its sides in a “fan-beam” pattern that is directed perpendicular to the magnetic field. For $L_X \lesssim L_{crit}$ instead matter falls almost freely up to the NS surface, causing the braking of the plasma by a hydrodynamical shock. X-rays in this case can escape vertically along the accretion column, producing a "pencil-beam" pattern.

More recent considerations also predict that a fraction of the fan-beam emission can be reflected off the surface of the NS, producing a secondary polar beam that is directed parallel to the magnetic field axis in a "pencil-beam" model (Poutanen et al. 2013).

The emission of the accretion column of XRPs has a spectrum that is empirically described by a very hard power law (spectral index $\lesssim 1.8$) with a low-energy ($\lesssim 10$ keV) cut-off (Caballero & Wilms 2012). It has been demonstrated that the spectrum can be reproduced assuming thermal Comptonization of bremsstrahlung, blackbody, and cyclotron seed photons (Nagel 1981). However no self consistent, general model has been found due to the complexity of the physical processes both in the accretion column and in the magnetosphere. A better and complete description of the scattering processes, which are the dominant processes inside these structures, would help to discriminate between various models for the emitting region.

Chapter 2

Radiation in strong magnetic fields

The motion of the charged particles in the presence of a strong magnetic field is strongly anisotropic: they are free to move along the magnetic field direction while they are confined in quantized orbits perpendicularly to it. The propagation of radiation in this magnetized medium depends on the polarization modes of photons which are expected to be linearly polarized in two normal modes, ordinary and extraordinary. Strong magnetic fields can also influence the propagation of photons in vacuo, producing an increase of the observed linear polarization (Heyl & Shaviv 2002, Taverna et al. 2015).

In this chapter we firstly describe the motion of an electron both in the limits of weak field (2.1.1) and strong field (2.1.2). Then in section 2.2.1 we describe the photon propagation and polarization modes in a magnetized plasma together with vacuum polarization effects. Finally in section 2.2.2 we introduce the Stokes parameters both for a single photon and the entire radiation.

2.1 Matter in strong magnetic fields

2.1.1 Weak field case

The equation of motion of an electron in a uniform, static magnetic field $\boldsymbol{B}$ is

$$\frac{d}{dt}(m\gamma\boldsymbol{v}) = \frac{e}{c}(\boldsymbol{v}\times\boldsymbol{B}), \tag{2.1}$$

with m rest mass of the electron, $\boldsymbol{v}$ its velocity and e its charge; $\gamma = (1 - v^2/c^2)^{-1/2}$ is the Lorentz factor. The first term in eq. 2.1 can be expanded as

$$\frac{d}{dt}(m\gamma\boldsymbol{v}) = m\frac{d}{dt}(\gamma\boldsymbol{v}) = m\gamma\frac{d\boldsymbol{v}}{dt} + m\gamma^3\boldsymbol{v}\frac{\boldsymbol{v}\cdot\boldsymbol{a}}{c^2}, \tag{2.2}$$

with $\boldsymbol{a} = d\boldsymbol{v}/dt = \boldsymbol{F}_L/m$ where $\boldsymbol{F}_L = e/c\,(\boldsymbol{v}\times\boldsymbol{B})$ is the Lorentz force, from which we see that $\boldsymbol{a}$ and $\boldsymbol{v}$ are always perpendicular, then $\boldsymbol{v}\cdot\boldsymbol{a} = 0$ and equation 2.1 becomes

$$\gamma m\frac{d\boldsymbol{v}}{dt} = \frac{e}{c}(\boldsymbol{v}\times\boldsymbol{B}). \tag{2.3}$$

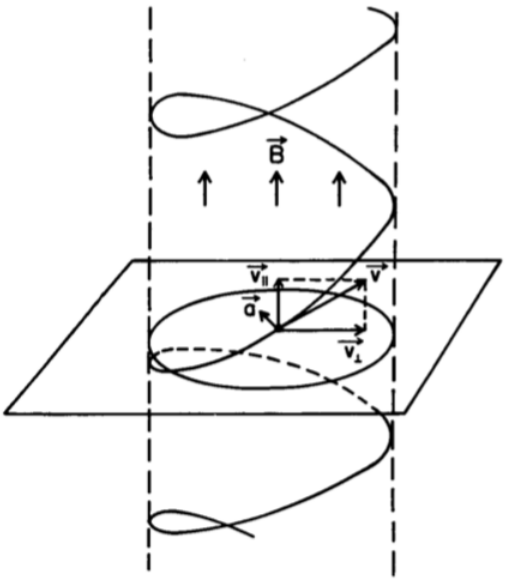

Figure 2.1: Motion of an electron in a static, uniform magnetic field along z (Mészáros 1992).

Introducing the velocity components $v_\parallel$ and $v_\perp$, parallel and perpendicular to the field, respectively, we have

$$\gamma m \frac{dv_\parallel}{dt} = \frac{e}{c}(\boldsymbol{v}_\parallel \times \boldsymbol{B}) = 0 \Rightarrow \frac{dv_\parallel}{dt} = 0 \Rightarrow v_\parallel = const. \tag{2.4}$$

Being the only acting force the Lorentz force, which is perpendicular to the electron velocity, $|\boldsymbol{v}| = cost$ and since $\left|\boldsymbol{v}_\parallel\right| = const$ then also $|\boldsymbol{v}_\perp| = const$. Therefore particles move with a uniform, circular motion in the plane perpendicular to the $\boldsymbol{B}$ field and with a constant motion along z. This results in an helicoidal motion with a constant angle θ between the field and the velocity as illustrated in Figure 2.1. Equating the equation of motion with the circular motion equation we can infer the radius of the circular motion:

$$\frac{v_\perp^2}{r_L} = \frac{e}{c}\frac{v_\perp \mid \boldsymbol{B} \mid}{\gamma m} \Rightarrow r_L = \frac{m\gamma c v_\perp}{eB}, \tag{2.5}$$

which is called the Larmor or cyclotron radius. The angular frequency is

$$\omega_c = \frac{eB}{m\gamma c}. \tag{2.6}$$

2.1.2 Strong field case

In a strong magnetic field ($B \gtrsim 10^{12} - 10^{13}$ G) a quantum treatment is necessary since r_L becomes comparable to or smaller than the de Broglie wavelength of the electron $\lambda_B = \hbar/p$, with p the electron momentum. Moreover, the electron motion perpendicular to the magnetic field results quantized.

Quantum effects become important when

$$\frac{\hbar}{\gamma m v} \geq \frac{\gamma m c v_\perp}{eB} \tag{2.7}$$

which corresponds to a magnetic field

$$B \geq \frac{m^2c^3\gamma^2}{e\hbar}\Big(\frac{v_\perp}{c}\Big)^2 = \gamma^2\beta_\perp^2 B_Q, \tag{2.8}$$

where B_Q is the critical magnetic field (or Schwinger magnetic field)

$$B_Q = \frac{m^2c^3}{e\hbar} = 4.413 \times 10^{13}\text{G}. \tag{2.9}$$

The classical cyclotron energy at $B = B_Q$ becomes equal to the electron rest mass energy mc^2

$$\varepsilon_c = \hbar\omega_c = \hbar\frac{eB}{mc} = mc^2(B/B_Q). \tag{2.10}$$

and, setting $r_L = \lambda_B$, we obtain a characteristic magnetic quantum length scale for the electron

$$\gamma mvc/eB = \lambda \Rightarrow \hbar c/eB = \lambda$$

$$\Rightarrow \lambda = (\hbar c/eB)^{1/2} = 2.6 \times 10^{-10} B_{12}^{1/2}\text{cm}\,, \tag{2.11}$$

where B is in units of 10^{12} G.

As in the classical limit, electrons move with a circular motion of frequency ω_c in the plane perpendicular to $\boldsymbol{B}$ and with a free constant motion along $\boldsymbol{B}$. In the zero spin case, the energy levels are

$$\begin{aligned} E &= (n+1/2)\hbar\omega_c + (1/2m)p_z^2 \\ &= (n+1/2)mc^2(B/B_Q) + (1/2m)p_z^2, \qquad n = 0, 1, \ldots \end{aligned} \tag{2.12}$$

i.e. a spectrum composed by a continuum along z and a discrete set of levels in the transverse direction called Landau levels. They differ from the classical ones by the factor $1/2$ which is due to the zero-point energy of the ground state $n = 0$ which is $1/2mc^2(B/B_Q)$. The circular orbits have also quantized radii

$$r_n = (2n)^{1/2}\lambda \tag{2.13}$$

with λ given by 2.11.

If we include the contribution of the spin term, eq. 2.12 becomes

$$E = \frac{1}{2}\hbar\omega_c(2n + 1 + \zeta) + (1/2m)p_z^2 \qquad n = 0, 1, \ldots \qquad \zeta = \pm 1, \tag{2.14}$$

where ζ are the spin eigenvalues. The relativistic generalization, obtainable by solving the Dirac equation, is

$$\begin{aligned} E &= [m^2c^4 + c^2p_z^2 + (2n + \zeta + 1)mc^2\hbar\omega_c]^{1/2} = \\ &= [m^2c^4 + c^2p_z^2 + (2n + \zeta + 1)m^2c^4(B/B_Q)]^{1/2}\,. \end{aligned} \tag{2.15}$$

2.2 X-ray Polarimetry

So far, X-ray sources has been studied only through spectral characteristics and time variabilities. Even if lot has been achieved in our understanding of X-ray objects in this way, it is not enough to have a full understanding of these sources. Different conditions and combinations of the parameters of X-ray sources produce the same spectral characteristics which is why with the spectral analysis only is not possible to univocally define the geometry of these sources. Two more observables are needed: the direction and the magnitude of polarization which both can be obtained from polarimetry measurements. The great importance of polarimetry has been already emphasized (Soffitta et al. 2013): it could lead to a better understanding of the rotation-powered and accretion-powered pulsar radiation mechanisms; it could help to determine the geometry and the emission mechanism of Active Galactic Nuclei and micro-quasars, to find the magnetic field configuration in magnetars and to determine the magnitude of the field, to find the mechanism for X-ray production in pulsars (both isolated and accreting) and the geometry, to determine how particles are accelerated in Pulsar Wind Nebulae, Supernova Remnants and Jets, to test fundamental physics from quantum effects to quantum gravity and much more.

2.2.1 Photon propagation in a magnetized plasma

In the reference frame (x, y, z) with $\boldsymbol{k}$ along the z-axis, and the x-axis in the $\boldsymbol{k} - \boldsymbol{B}$ plane, the electric field of a photon can be written as

$$\boldsymbol{E} = E_0(z)e^{-i\omega t} = \boldsymbol{A}(z)e^{i(k_0 z - \omega t)}, \tag{2.16}$$

with $k_0 = \omega/c$ and $\boldsymbol{A} = (A_x, A_y, A_z)$ is the electric field complex amplitude. Maxwell wave equation describes the evolution of the electric field of the photon

$$\boldsymbol{\nabla} \times (\bar{\boldsymbol{\mu}} \cdot \boldsymbol{\nabla} \times \boldsymbol{E}) = \frac{\omega^2}{c^2} \boldsymbol{\epsilon} \cdot \boldsymbol{E} \tag{2.17}$$

where $\boldsymbol{\mu}$ is the magnetic permeability tensor and $\boldsymbol{\epsilon}$ is the dielectric tensor. In a cold electron-ion plasma under an external magnetic field $\boldsymbol{B}$, electrons and ions (with charge, mass and number density given by $-e$, m_e, n_e and Ze, m_i, n_i respectively) are coupled by collisions with frequency ν_{ei} and have radiative damping frequencies ν_{re} and ν_{ri} respectively. The dielectric tensor, in the reference frame with $\boldsymbol{B}$ along z, is given by (Harding & Lai 2006)

$$\boldsymbol{\epsilon}^{(\boldsymbol{p})} = \begin{bmatrix} \varepsilon & ig & 0 \\ -ig & \varepsilon & 0 \\ 0 & 0 & \eta \end{bmatrix} \tag{2.18}$$

where

$$\begin{aligned} \varepsilon \pm g &= 1 - \frac{1}{\omega} \frac{\omega_p^2(\omega + i\nu_{ei}) + \omega_{pi}^2(\omega + i\nu_{re})}{(\omega + i\nu_{re} \pm \omega_c)(\omega + i\nu_{ri} \mp \omega_{ci}) + i\omega\nu_{ei}} \\ \eta &\simeq 1 - \frac{1}{\omega}\left(\frac{\omega_p^2}{\omega + i(\nu_{ei} + \nu_{re})} - \frac{\omega_{p,i}^2}{\omega + i(\nu_{ei} + \nu_{ri})}\right). \end{aligned} \tag{2.19}$$

with $\omega_{pe} = (4\pi n_e e^2/m_e)^{1/2}$ is the electron plasma frequency, $\omega_{pi} = (4\pi n_i Z^2 e^e/m_i)^{1/2}$ is the ion plasma frequency, $\omega_c = eB/(m_e c)$ is the electron cyclotron frequency and $\omega_{ci} = ZeB/(m_i c)$ is the ion cyclotron frequency. The damping frequencies ν_{ei}, ν_{re} and ν_{ri} are given by

$$\begin{aligned}
\nu_{ei} &= \frac{Z^2 n_i e^4}{\hbar\omega}\left(\frac{2\pi}{m_e kT}\right)^{1/2}(1-e^{-\hbar\omega/kT})g_\alpha^{ff}, \\
\nu_{re} &= \frac{2e^2\omega^2}{3m_e c^3}, \\
\nu_{ri} &= \frac{Z^2 m_e \omega}{m_i}\gamma_{re}.
\end{aligned} \tag{2.20}$$

where g_α^{ff} is the Gaunt factor (Potekhin & Chabrier 2003).

Strong magnetic fields influence not only the behavior of matter but also photon propagation in vacuum. According to quantum electrodynamics, the vacuum is filled with virtual electron-positron pair which can be then polarized by the strong magnetic field. Thus in the magnetized vacuum the dielectric and magnetic permeability tensors depart from unity, altering the radiative scattering and absorption opacities (Mészáros & Ventura 1979; Pavlov & Gnedin 1984). Vacuum polarization becomes significant when $b = B/B_Q \gtrsim 1$, which occurs in many NSs. The contribution of vacuum polarization to the dielectric tensor is

$$\boldsymbol{\epsilon}^{(v)} = a\mathbb{1} + q\hat{\boldsymbol{B}}\hat{\boldsymbol{B}} \tag{2.21}$$

where $\hat{\boldsymbol{B}}$ is the local magnetic field unit vector and the inverse magnetic permeability tensor is given by

$$\bar{\boldsymbol{\mu}}^{(v)} = a\mathbb{1} + m\hat{\boldsymbol{B}}\hat{\boldsymbol{B}}. \tag{2.22}$$

where a, q and m are function of b (Harding & Lai 2006). For $\hbar\omega \ll m_e c^2$, a good approximation for the coefficients a, q and m is given by Potekhin et al. (2004):

$$\begin{aligned}
a &\approx -\frac{2\alpha_F}{9\pi}\ln\left(1+\frac{b^2}{5}\frac{1+0.25487b^{3/4}}{1+0.75b^{5/4}}\right) \\
q &\approx \frac{7\alpha_F}{45\pi}b^2\frac{1+1.2b}{1+1.33b+0.56b^2} \\
m &\approx -\frac{\alpha_F}{3\pi}\frac{b^2}{3.75+2.7b^{5/4}+b^2}.
\end{aligned} \tag{2.23}$$

In the limit of weak field, $b \ll 1$, these coefficients are given by (Adler 1971)

$$a = -\frac{2\alpha_F}{45\pi}b^2, \quad q = \frac{7\alpha_F}{45\pi}b^2, \quad m = -\frac{4\alpha_F}{45\pi}b^2 \tag{2.24}$$

where α_F is the fine structure constant.

For $B \ll 5\times10^{16}$ G, the plasma and vacuum contributions of eq. 2.18 and 2.21 can be summed linearly to obtained the total dielectric tensor $\boldsymbol{\epsilon}$ (Ho & Lai 2003) which results in

$$\boldsymbol{\epsilon} = \begin{bmatrix} \varepsilon' & ig & 0 \\ -ig & \varepsilon' & 0 \\ 0 & 0 & \eta' \end{bmatrix} \tag{2.25}$$

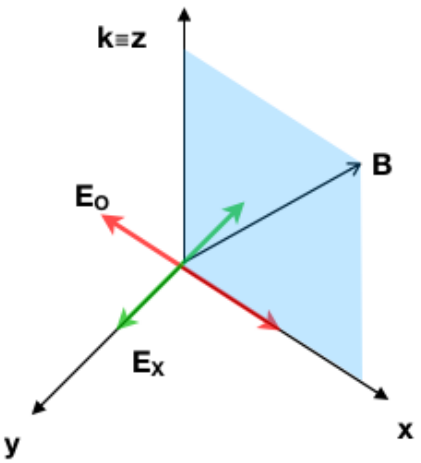

Figure 2.2: Reference system for the polarization modes. The unit vectors E_X and E_O along which the electric field two modes (X- and O-mode) oscillate are also shown.

where $\varepsilon' = \varepsilon + a$ and $\eta' = \eta + a + q$. The inverse total magnetic permeability tensor instead remains as in eq. 2.22.

The polarization modes are found more easily in the reference system with $\boldsymbol{k}$ along the z-axis and $\boldsymbol{B}$ in the $x - z$ plane, such that $\hat{\boldsymbol{B}} \times \hat{\boldsymbol{k}} = \sin\theta_B \hat{\boldsymbol{y}}$, with θ_B the angle between $\boldsymbol{k}$ and $\boldsymbol{B}$ (Figure 2.2). For normal modes propagating with $\boldsymbol{E} \propto e^{ik_j z}$, eq. 2.17 reduces to

$$- k_j^2 \hat{z} \times [\bar{\boldsymbol{\mu}} \cdot (\hat{z} \times \boldsymbol{E}_j)] = \frac{\omega^2}{c^2} \boldsymbol{\epsilon} \cdot \boldsymbol{E}_j, \tag{2.26}$$

where the subscripts $j = 1, 2$ specify the two modes. Solving the wave equation in this reference system we obtain the unit vector along which the electric field of the two modes oscillate

$$\hat{E}_j = \frac{1}{\sqrt{1 + K_j^2 + K_{z,j}^2}} \begin{pmatrix} iK_j \\ 1 \\ iK_{z,j} \end{pmatrix} \tag{2.27}$$

where $K_{zj} = iE_z/E_y$ and $K_j = -iE_x/E_y$ is the mode ellipticity given by Ho & Lai (2003):

$$K_j = \beta \pm \sqrt{\beta^2 + r} \tag{2.28}$$

with $r = 1 + [m/(1+a)] \sin^2\theta_B \simeq 1$ and the polarization parameter β

$$\beta = -\frac{\varepsilon'^2 - g^2 - \varepsilon'\eta'(1 + m/a)}{2g\eta'} \frac{\sin^2\theta_B}{\cos\theta_B}. \tag{2.29}$$

The polarization parameter determines the properties of photon normal modes in the medium. The refractive index $n_j = ck_j/\omega$ is given by

$$n_j^2 = \frac{g\eta'}{a(\varepsilon' \sin^2\theta_B + \eta' \cos^2\theta_B)} \left(\frac{\varepsilon'}{g} + \frac{1}{K_j} \cos\theta_B \right). \tag{2.30}$$

Thus, different polarization modes, both in plasma and in vacuum, lead to different values of the refractive index, producing what is called birefringence.

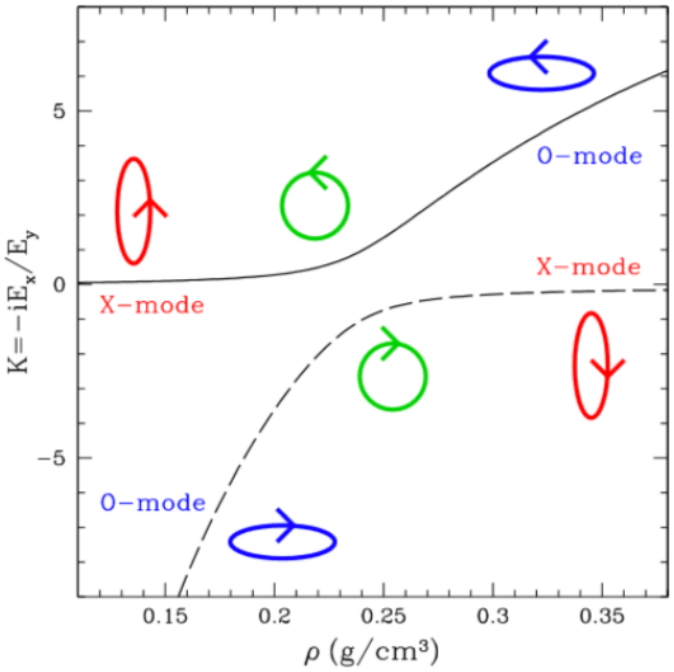

Figure 2.3: Plot of the mode ellipticity K as a function of the plasma density ρ for two photons close to the vacuum resonance, one emitted in O-mode (solid line) and one in X-mode (dashed line), with $\hbar\omega = 5$ keV, $\theta_B = 45°$, $B = 10^{13}$ G and $Y_e = 1$ (Harding & Lai 2006).

For general values of the photon energy, $|\beta| \gg 1$ so that the two modes are linearly polarized: mode 1, which is called extraordinary (X), has $|K| \ll 1$ and its electric field is almost perpendicular to the $\boldsymbol{k} - \boldsymbol{B}$ plane; while mode 2, which is called ordinary (O), has $|K| \gg 1$ and its electric field is in the $\boldsymbol{k} - \boldsymbol{B}$ plane. X- and O-mode photons interact very differently with matter: the O-mode scattering opacity is largely unaffected by the magnetic field, while the X-mode one is significantly reduced (by a factor of the order $(\omega/\omega_c)^2$) because of the strong confinement of electrons perpendicular to the magnetic field (Harding & Lai 2006). So O-mode photons are trapped inside the magnetized medium while X-mode photons can escape.

The condition $\beta = 0$ specifies the resonance points, which occurs when plasma and vacuum polarization effects equilize each other. At this point $K_j \approx 1$ so both modes are circularly polarized. The vacuum resonance for energies lower than $\hbar\omega_c$ and not to close to $\hbar\omega_{ci}$ is located at $\omega = \omega_p/\sqrt{q+m}$. This leads to a condition for the plasma density

$$\rho_V \simeq 0.964 Y_e^{-1} \left(\frac{\hbar\omega}{1\text{keV}}\right)^2 \left(\frac{B}{10^{14}\text{G}}\right)^2 \lambda^{-2} \text{gcm}^{-3}, \tag{2.31}$$

in which Y_e is the plasma electron fraction and $\lambda \simeq 1$ is a slow varying function of B (see Harding & Lai 2006). In Figure 2.3 the evolution of X- and O-mode of two photons, with energies $\hbar\omega$ emitted from the NS surface with $\theta_B = 45°, B = 10^{13}$ G and $Y_e = 1$ and propagating close to the vacuum resonance, is shown. For density $\rho \gtrsim \rho_V$, the plasma term dominates over the vacuum term and the normal modes are almost linearly polarized in their initial modes. Decreasing ρ, K approaches 1 up to $\rho = \rho_V$. Here the two modes are exactly circularly polarized, the O-mode

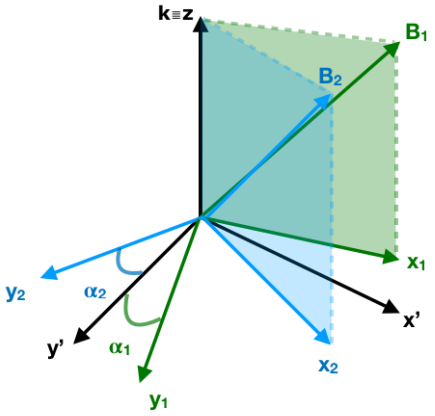

Figure 2.4: Graphic representation of the reference frames for different photons, with the common propagation direction $\boldsymbol{k}$.

is left-handed, the X-mode is right-handed. Passing to $\rho \lesssim \rho_V$ O-mode can convert in X-mode and viceversa, and the polarization returns again to be nearly linear when vacuum polarization term dominates.

2.2.2 Stokes parameters

Another way to describe the polarization of the radiation is through the Stokes parameters, which are a combination of the electric field complex amplitude components A_i from eq. 2.16. In the reference frame (x, y, z) with z along $\boldsymbol{k}$ and x in the $\boldsymbol{k} - \boldsymbol{B}$ plane as in Figure 2.4, the Stokes parameters for one photon are

$$\begin{aligned} \mathcal{I} &= A_x A_x^* + A_y A_y^* = a_x^2 + a_y^2 \\ \mathcal{Q} &= A_x A_x^* - A_y A_y^* = a_x^2 - a_y^2 \\ \mathcal{U} &= A_x A_y^* + A_y A_x^* = 2 a_x a_y \cos(\psi_x - \psi_y) \\ \mathcal{V} &= i(A_x A_y^* - A_y A_x^*) = 2 a_x a_y \sin(\psi_x - \psi_y) \end{aligned} \tag{2.32}$$

where a and ψ are related to A by

$$A_x = a_x e^{-i\psi_x}, \qquad A_y = a_y e^{-i\psi_y}. \tag{2.33}$$

$\mathcal{I}$ describe the total intensity, $\mathcal{Q}$ the strength of linear polarization while $\mathcal{U}$ the orientation in the $x - y$ plane of the polarization vector and $\mathcal{V}$ the circular polarization. The set of Stokes parameters defined for each photon fulfills the relation

$$\mathcal{I}^2 = \mathcal{Q}^2 + \mathcal{U}^2 + \mathcal{V}^2. \tag{2.34}$$

We can associate to the ordinary and extraordinary photons the Stokes vectors. Since for O-mode $a_y = 0$ and for the X-mode $a_x = 0$ it results

$$\begin{pmatrix} \bar{\mathcal{Q}} \\ \bar{\mathcal{U}} \\ \bar{\mathcal{V}} \end{pmatrix}_O = \begin{pmatrix} 1 \\ 0 \\ 0 \end{pmatrix} \qquad \begin{pmatrix} \bar{\mathcal{Q}} \\ \bar{\mathcal{U}} \\ \bar{\mathcal{V}} \end{pmatrix}_X = \begin{pmatrix} -1 \\ 0 \\ 0 \end{pmatrix} \tag{2.35}$$

where the bars denote the normalized Stokes parameters with respect to the photon intensity.

The major advantage of the Stokes parameters is that they are additive, so the collective Stokes parameters for the entire radiation are simply the sum of the ones of single photons. Combinations of the Stokes parameters define some observables for the entire radiation which can be measured by polarimeters: the linear polarization fraction Π_L, the polarization angle χ_p and the circular polarization fraction Π_C respectively defined as

$$\begin{aligned} \Pi_L &= \frac{\sqrt{Q^2 + U^2}}{I} \\ \chi_p &= \frac{1}{2} \arctan\left(\frac{U}{Q}\right) \\ \Pi_C &= \frac{V}{I}. \end{aligned} \tag{2.36}$$

Π_L represents the fraction of the total number of photons polarized in one of the two modes. χ_p represents the inclination of the polarization vector in the plane orthogonal to the line of sight and Π_C represents the fraction of the total number of photons circularly polarized. As seen, in presence of a strong magnetic fields photons are linearly polarized either in the X- or O-mode. Since in the reference frame as Figure 2.4, X-mode has $a_x = 0$ and O-mode has $a_y = 0$, $\mathcal{V}$ being $\propto a_x a_y$, it is always 0. Therefore in the vacuum $V = 0$ and circular polarization can be neglected.

Chapter 3

Radiation transport in strongly magnetized media

The transfer equation provides a useful phenomenological formalism which allows to solve for the specific intensity in an absorbing and emitting medium. First of all, we define some important quantities that describe radiation and physical processes in a medium. The energy dE_ω carried by the radiation field with frequency between ω and $\omega + d\omega$ which crosses an infinitesimal surface of area dA in the time dt and solid angle $d\Omega$ (Figure 3.1) is

$$dE_\omega = I_\omega \cos\theta dA d\omega d\Omega dt, \tag{3.1}$$

where $\cos\theta = \boldsymbol{n} \cdot \boldsymbol{k}$ with $\boldsymbol{n}$ the surface normal of dA and $\boldsymbol{k}$ the radiation direction, and $I_\omega(x, y, z, \theta, \phi, \omega, t)$ the specific intensity. Normally the time dependence is negligible since the characteristic time over which radiation evolves is far smaller than the one of matter. If the radiation propagates in vacuum, the specific intensity remains constant along a ray, $dI_\omega/ds = 0$. Otherwise, there are three processes which modify the specific intensity: absorption, spontaneous emission and scattering. The emission process, which increases I_ω, is characterized by the monochromatic emission coefficient j_ω that is the energy produced per unit frequency,

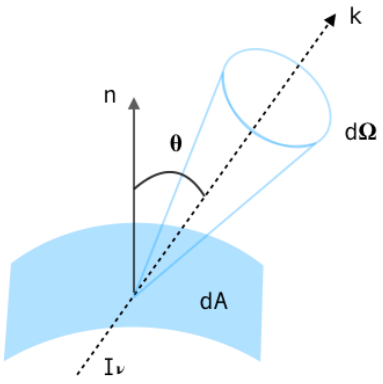

Figure 3.1: Specific intensity through a surface dA.

unit time and unit solid angle in an infinitesimal volume

$$dE^e_\omega = j_\omega dV d\Omega d\omega dt. \tag{3.2}$$

It depends only on the properties of matter and not on the incident radiation field. Similarly for absorption, which decreases I_ω, we introduce the monochromatic absorption coefficient α_ω that is defined by the phenomenological law

$$dE^a_\omega = -\alpha_\omega I_\omega dV d\Omega d\omega dt. \tag{3.3}$$

The scattering process can behave both as an absorption and emission process. When the photon is scattered, it is deviated from its original direction to a new one producing a decrease of the specific intensity in the original direction and an increase in the scattered one.

The scattering of a photon from $\boldsymbol{k}$ with frequency ω to $\boldsymbol{k}'$ with frequency ω' is described by the differential scattering cross section $d^2\sigma_s/(d\Omega' d\omega')$ which is the energy radiated per unit time per solid angle over the incident energy per unit time per unit area. The scattering process can produce an increase in the radiation field of

$$dE^+_{\omega,s} = d\Omega d\omega dt n_e dV \int \frac{d^2\sigma_s}{d\Omega' d\omega'}(\omega' \to \omega)\frac{\omega}{\omega'} I_{\omega'} d\Omega' d\omega' \tag{3.4}$$

considering all the photons which, coming from all the other directions, are scattered into $\boldsymbol{k}$ direction. It can produce a decrease of

$$dE^-_{\omega,s} = -d\Omega d\omega dt n_e dV I_\omega \int \frac{d^2\sigma_s}{d\Omega' d\omega'}(\omega' \to \omega) d\Omega' d\omega' = -d\Omega d\omega dt n_e dV I_\omega \sigma_s(\omega) \tag{3.5}$$

since the radiation from $\boldsymbol{k}$ direction is scattered to other directions and so it is lost. Considering all these contributions we obtain the radiation transport equation (RTE) in a medium for one mode:

$$\frac{dI_\omega}{ds} = j_\omega - (\alpha_\omega + n_e\sigma_s)I_\omega + \int n_e I_{\omega'} \frac{\omega}{\omega'} \frac{d^2\sigma_s}{d\Omega' d\omega'}(\omega' \to \omega) d\Omega' d\omega'. \tag{3.6}$$

For both the NS surface and accretion column, a good approximation that can be used for solving RTE is the plane parallel assumption for which properties of matter and radiation depend only on the depth in the medium. It is convenient to use $\mu_B = \cos\theta_B$, (θ_B is the angle between the photon propagation and $\boldsymbol{B}$) and calculate the transfer equation with respect to dz instead of the photon propagation direction ds which are linked by the relation $dz = \mu_B ds$.

It is the last term of the eq. 3.6 that, making the RTE an integro-differential equation, complicates the problem. It can be solved only with numerical techniques. If we assume that the scattering is coherent ($\omega = \omega'$) and the cross section is isotropic, so in the limit of Thomson scattering, RTE is easier to solve. In this case, being the cyclotron energy typically above the photon energies, the scattering is non-resonant and the differential scattering cross section has

been calculated for each mode (Taverna & Turolla 2017):

$$\begin{aligned}
\frac{d^2\sigma_{OO}}{d\varepsilon' d\Omega'}(\alpha \to \alpha') &= \frac{3}{8\pi}\sigma_T(1-\mu_B^2)(1-\mu_B'^2) \\
\frac{d^2\sigma_{OX}}{d\varepsilon' d\Omega'}(\alpha \to \alpha') &= \frac{3}{8\pi}\sigma_T\left(\frac{\varepsilon}{\varepsilon_c}\right)^2 \mu_B^2\cos^2(\phi_B-\phi_B') \\
\frac{d^2\sigma_{XO}}{d\varepsilon' d\Omega'}(\alpha \to \alpha') &= \frac{3}{8\pi}\sigma_T\left(\frac{\varepsilon}{\varepsilon_c}\right)^2 \mu_B'^2\cos^2(\phi_B-\phi_B') \\
\frac{d^2\sigma_{XX}}{d\varepsilon' d\Omega'}(\alpha \to \alpha') &= \frac{3}{8\pi}\sigma_T\left(\frac{\varepsilon}{\varepsilon_c}\right)^2 \sin^2(\phi_B-\phi_B')
\end{aligned} \tag{3.7}$$

where ε and ε_c are respectively the energy of the incoming photon and the cyclotron energy, μ_B and μ_B' are the cosine of the angle θ_B and θ_B' and ϕ_B and ϕ_B' are the associated azimuthal angles. As we can see, photons can convert their polarization mode upon scattering. Moreover, the cross sections of X-mode photons are proportional to a factor $(\varepsilon/\varepsilon_c)^2$ for which we can see that it is strongly reduced as much as the magnetic field increases, being $\omega_c \propto B$ and so the X-mode photon cross sections decrease with B^{-2}. So the medium becomes optically thin for X-mode photons while for O-mode photons the cross resembles the Thomson cross section. Because of this difference in the behavior of the two modes, the RTE has to be separated in 2 equations, one for each mode. In a medium dominated by scattering (so $j_\omega = 0$ and $\alpha_\omega = 0$), the two RTEs for the two modes, in term of the photon number intensity n_i (i =O,X), are

$$\begin{aligned}
\mu_B\frac{dn_O}{d\tau} = \sum_{k=O,X}\int\Bigg\{&-\frac{d^2\sigma_{Ok}}{d\Omega' d\varepsilon'}(\alpha\to\alpha')n_O(\alpha)[1+n_k(\alpha')]+ \\
&\frac{d^2\sigma_{k,O}}{d\Omega' d\varepsilon'}(\alpha'\to\alpha)\left(\frac{\varepsilon'}{\varepsilon}\right)^2 n_k(\alpha')[1+n_O(\alpha)]\Bigg\}d\varepsilon' d\Omega' \\
\mu_B\frac{dn_X}{d\tau} = \sum_{k=O,X}\int\Bigg\{&-\frac{d^2\sigma_{Xk}}{d\Omega' d\varepsilon'}(\alpha\to\alpha')n_X(\alpha)[1+n_k(\alpha')]+ \\
&\frac{d^2\sigma_{k,X}}{d\Omega' d\varepsilon'}(\alpha'\to\alpha)\left(\frac{\varepsilon'}{\varepsilon}\right)^2 n_k(\alpha')[1+n_X(\alpha)]\Bigg\}d\varepsilon' d\Omega'
\end{aligned} \tag{3.8}$$

where $d\tau = \sigma_T n_e dz$ is the infinitesimal Thomson depth. In presence of local thermodynamic equilibrium, the scattering cross section must follow the detailed balance condition

$$\sigma_{ki}(\alpha'\to\alpha) = \left(\frac{\varepsilon}{\varepsilon'}\right)^2 \exp[-(\varepsilon-\varepsilon')/kT]\sigma_{ik}(\alpha\to\alpha')\,, \tag{3.9}$$

so eq. 3.8 becomes

$$\mu\frac{dn_i}{d\tau} = \sum_{k=O,X}\int\Big\{-\sigma_{ik}(\alpha\to\alpha')n_i(\alpha)+\sigma_{ik}(\alpha\to\alpha')F_i(\alpha,\varepsilon')n_k(\alpha')\Big\}d\varepsilon' d\Omega'\,, \tag{3.10}$$

where $F_i(\alpha,\varepsilon') \equiv \exp[-(\varepsilon-\varepsilon')/kT](1+n_i(\alpha)) - n_i(\alpha)$.

In case of strong magnetic fields and high energies, in which the limit of Thomson scattering is no longer valid, the radiative transfer equation takes the same form as 3.8 but with σ_{ij} calculated for the Compton scattering process. To calculate the total cross section σ_s it is

necessary to perform a numerical integration over the different outgoing angles and frequencies. This problem can be partially avoided using the optical theorem which links the total scattering cross section with the imaginary part of the forward scattering amplitude $\Pi(0)$

$$\sigma_s = \frac{4\pi}{k} \operatorname{Im} \Pi(0) \tag{3.11}$$

where k is the photon momentum. Using QED, it is possible to calculate $\Pi(0)$, so that σ_s can be immediately obtained.

Still the problem of integrals remains in the last term of 3.6 where the differential scattering cross section multiplied by the specific intensity has to be integrated over all the outgoing angles and frequencies. In previous works this has been overpassed using the two-stream approximation, i.e. assuming that the entire radiation field can be represented by radiation traveling at just two angles. In this way the problem is greatly simplified but it is no more representative of a highly angle-dependent problem of the magnetic scattering, which will be deeply analyzed in next chapter.

Chapter 4

Compton scattering

In many high-energy astrophysical objects, one of the most important radiative processes is Compton scattering. In particular inside accretion columns it is the largest source of opacity. This process strongly affects the spectra of various sources since it produces photon wavelength changes which alter the initial spectral distribution. While non magnetic scattering has been thoroughly studied and a complete description is available, the magnetic scattering is still an open issue.

Strong external magnetic fields significantly affect the properties of scattering (Harding & Lai 2006). As seen in chapter 2.1 electrons are constrained to move in fixed and quantized orbits determined by the field strength and to follow magnetic field lines. Cross section becomes strongly dependent on energy, direction of photon momentum and polarization (in term of the two polarization modes, O- and X-mode) and on the magnetic field strength. A number of resonances corresponding to electron transitions between the Landau levels appear and their values may far exceed the Thomson scattering cross section. These particular features of the differential scattering cross section make the numerical implementation more complicated with respect of the non-magnetic case.

In section 4.1 we introduce the scattering process in absence of magnetic field in the Thomson and Compton limits. In section 4.2 we introduce the magnetic scattering using the formalism by Nagel (1981) and Mészáros (1992) which is then analyzed in chapter 5.

4.1 Non-magnetic scattering

Depending on the energies involved, there are two kinds of processes: Thomson scattering in which the photon energy $\hbar\omega$ is far lower than the electron rest-mass $m_e c^2$ and Compton scattering in which $\hbar\omega \gtrsim m_e c^2$.

Thomson scattering can be treated in the classical electromagnetic theory because it applies in the limit of $m_e c^2 \gg h\omega$. It can be considered as an elastic scattering because there is no energy exchange between the two particles. The electric field of the incident wave (photon) accelerates the electron, that can be considered at rest, causing it to radiate at the same frequency of

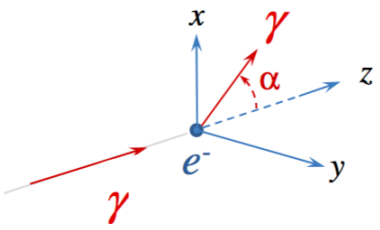

Figure 4.1: Thomson scattering geometrical configuration. Without loss of generalization, the scattering is assumed here to occur in the $x-z$ plane, with α the angle between the scattered photon and the z-axis.

the incident wave in any directions. The electron will oscillate along the photon electric field, emitting electromagnetic dipole radiation which turns out to be polarized even if the incident radiation was unpolarized. The differential scattering cross-section is the ratio between the energy radiated per unit time per unit solid angle (calculated with the Larmor formula) and the incident energy per unit time per unit area (described by the average Pointing vector). For Thomson scattering it is

$$d\sigma_T = \frac{r_0^2}{2}(1+\cos^2\alpha)d\Omega, \tag{4.1}$$

where α is the angle between the direction of the scattered photon and that of the incident photon, see Figure 4.1. As we can see, the differential Thomson cross section just depends on the scattering direction α. Integrating over the solid angle we find the Thomson cross-section for scattering onto electrons,:

$$\sigma_T = \frac{8\pi}{3}r_0^2 = \frac{8\pi e^4}{3m_e^2c^4} \sim 6.65\times10^{-25}\text{cm}^2. \tag{4.2}$$

σ_T does not depend on the frequency, so high- and low-frequency photons are equally efficiently scattered.

To explain the shift in wavelengths for Compton scattering, it is necessary to consider the electromagnetic radiation not as a pure wave phenomenon but as a stream of photons which exchange energy and momentum.

When the energy of the incident photon becomes comparable to the rest-mass energy of the electron, upon scattering photon exchanges energy and momentum with the electron, causing an increase or decrease of the photon wavelength and the recoil of the electron. In a hot plasma, electrons cannot be considered at rest, so the electron velocity distribution must be introduced to describe the electron distribution. If after the scattering photons lose energy and electrons acquire it, the process is called Compton scattering, in the opposite case it is usually called Inverse Compton scattering.

It is common to introduce two reference frames: the laboratory frame in which the electron is moving with a velocity $\boldsymbol{v}$ along the z-axis as it is shown in Figure 4.2a; and the electron rest frame (ERF) in which the electron is at rest and which moves in a relative motion with relative velocity $\boldsymbol{v}$ (Figure 4.2b). The convenience of using two different frames is that the differential

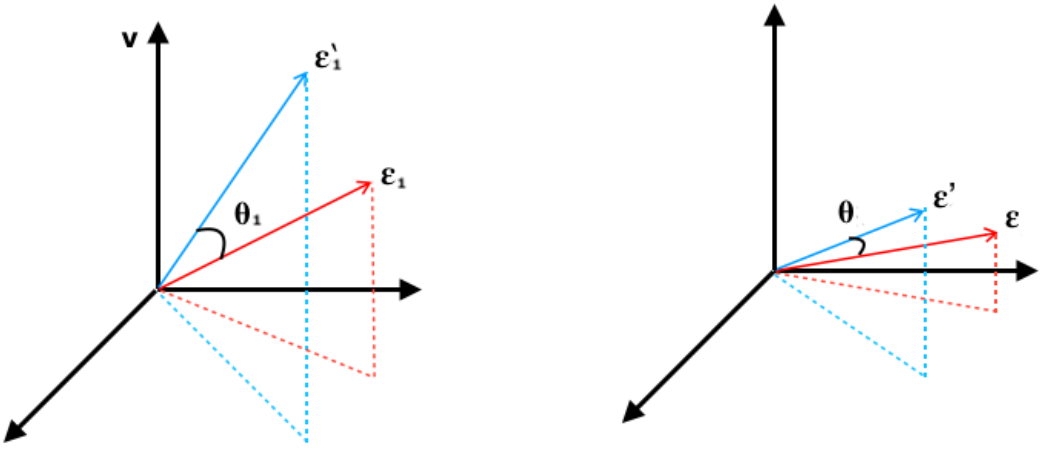

(a) *Laboratory frame.* (b) *Electron Rest Frame (ERF).*

Figure 4.2: Geometry of the Compton scattering.

cross section is easier to calculate in the ERF, while the electron and radiation distribution is known in the laboratory frame. It is possible to pass from a system to the other just with a Lorentz transformation. Calling $\varepsilon = \hbar\omega/m_e c^2$ the adimentional energy, with the "$\prime$" all the quantities after the scattering and with the subscript "1" all the quantities in the lab frame the differential scattering cross section is described by the Klein-Nishina formula:

$$\frac{d^2\sigma}{d\varepsilon' d\Omega'} = \frac{r_0^2}{2}\frac{\varepsilon'^2}{\varepsilon^2}\left(\frac{\varepsilon}{\varepsilon'} + \frac{\varepsilon'}{\varepsilon} - \sin^2\theta\right)\delta(\varepsilon' - \varepsilon_*), \tag{4.3}$$

where $\delta(x)$ is the Dirac delta function and

$$\varepsilon_* = \frac{\varepsilon}{1 + \varepsilon(1 - \cos\theta)}. \tag{4.4}$$

In the Thomson limit $\varepsilon_* = \varepsilon$ (coherent scattering), and so the differential cross section take the form of eq. 4.1. Eq. 4.3 can be integrated over the solid angle and outgoing photon energy and we find the total cross section and its asymptotic limits

$$\sigma_{KN} = \frac{\pi r_0^2}{\varepsilon}\left\{\left[1 - \frac{2(1-\varepsilon)}{\varepsilon^2}\right]\ln(1+2\varepsilon) + \frac{1}{2} + \frac{4}{\varepsilon} - \frac{1}{2(1+2\varepsilon)^2}\right\} \tag{4.5a}$$

$$= \sigma_T \times \begin{cases} 1 - 2\varepsilon + \dots & \varepsilon \ll 1 \\ \frac{3}{8\varepsilon}\left(\frac{1}{2} + \ln 2\varepsilon\right) + \dots & \varepsilon \gg 1. \end{cases} \tag{4.5b}$$

In Figure 4.3 we can see the two limits of the total cross section indicated in eq. 4.5b, for which for low energies $\sigma_{KN} \simeq \sigma_T$ while for high energies $\sigma_{KN} \propto 1/\varepsilon$.

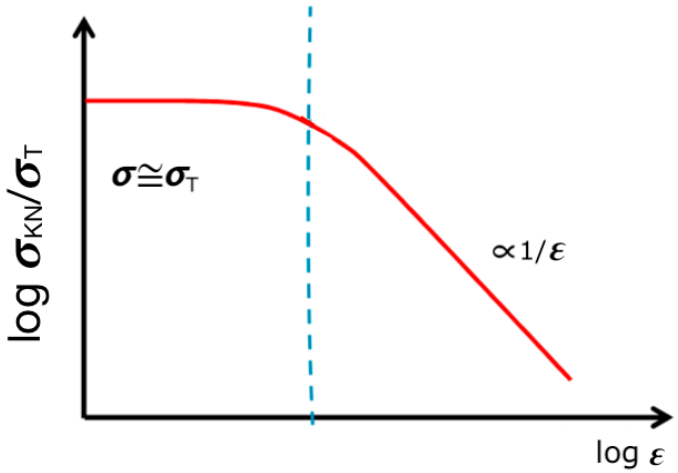

Figure 4.3: Plot of the total cross section given by Klein-Nishina formula. The dashed blue line divides the two regimes which correspond to the two limits at low and high energies.

4.2 Magnetic scattering

We follow the treatment used by Mészáros (1992) to describe the differential Compton scattering cross section in the magnetic scattering process in the non-relativistic case. For the sake of simplicity we will neglect the spin contribution and we will consider only the case in which before and after scattering the electron is in the ground Landau level, $n = n' = 0$. According to QED, the scattering process is described completely by its scattering matrix T, which contains the information about the probability amplitudes. It can be obtained starting from the perturbation Hamiltonian of an electron of momentum $\boldsymbol{p}$ by the incident photon of momentum $\boldsymbol{k}$ and electric field $\boldsymbol{A}$

$$T = H_1 + H_2 = \frac{e}{2c}(\boldsymbol{v} \cdot \boldsymbol{A} + \boldsymbol{A} \cdot \boldsymbol{v}) + \frac{e^2}{2mc^2}A^2. \tag{4.6}$$

The matrix elements which describes the scattering process are

$$\langle f \,|\, T \,|\, i \rangle = \frac{\sum_r \langle f \,|\, H_1 \,|\, r \rangle \langle r \,|\, H_1 \,|\, i \rangle}{E_i - E_r} + \langle f \,|\, H_2 \,|\, i \rangle \,, \tag{4.7}$$

where $|i\rangle = |0, s, 0\rangle$ is the initial state of the electron, $|f\rangle = |0, s', p'\rangle$ is its final state and $|r\rangle$ all the possible intermediate states that can have $n \neq 0$. The various states of the electron are characterized by three quantities: the Landau level n which is assumed 0, the spin number s and the electron momentum k.

In Thomson limit we can use the dipole approximation and so only three terms remain, T_a, T_b, T_c, which have $\Delta n = 0$ and which correspond to the Feynman's diagrams in Figure 4.4. T_a and T_b come from the first term in eq. 4.7, the first-order term, while the third one is from the

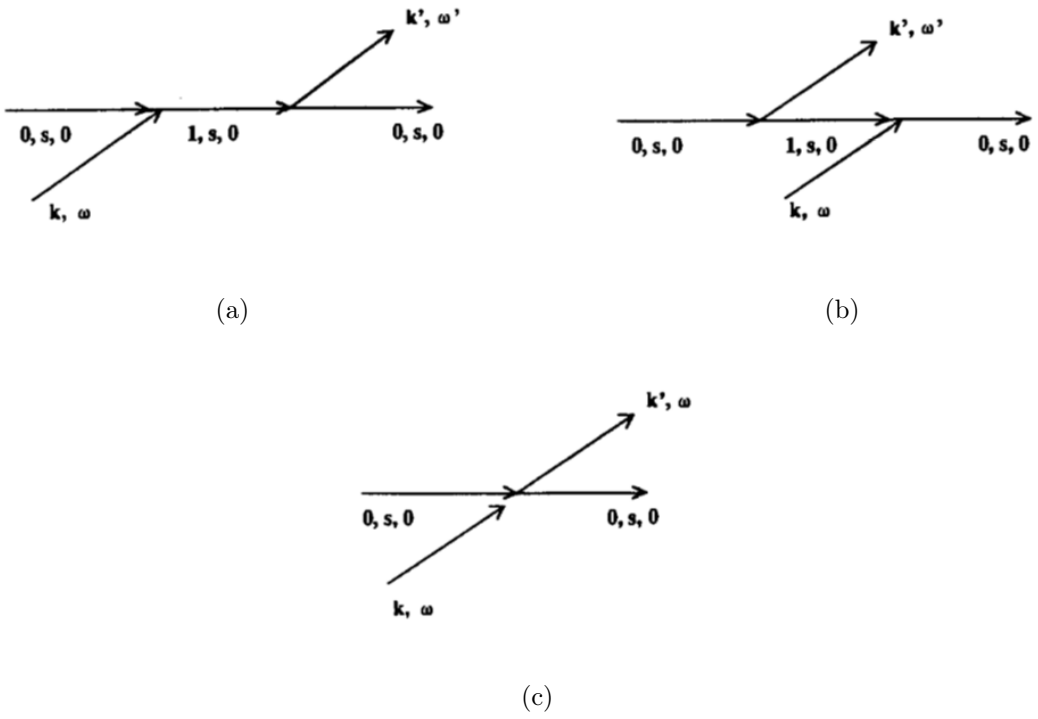

Figure 4.4: Feynman diagrams for Thomson scattering with $n = n' = 0$ (Mészáros 1992).

quadratic interaction in the second term

$$T_a = \frac{2\pi\alpha_F\hbar^2 c}{\omega L^3}\frac{(\hbar\omega_c/m)^{1/2}e'^*_-(\hbar\omega_c/m)^{1/2}e_-}{\hbar\omega - \hbar\omega_c} \tag{4.8a}$$

$$T_b = \frac{2\pi\alpha_F\hbar^2 c}{\omega L^3}\frac{(\hbar\omega_c/m)^{1/2}e_+(\hbar\omega_c/m)^{1/2}e'^*_+}{\hbar\omega - (\hbar\omega_c + 2\hbar\omega)} \tag{4.8b}$$

$$T_c = \frac{2\pi\alpha_F\hbar^2 c}{\omega L^3}(e'^*_+e_+ + e'^*_-e_- + e'^*_z e_z) \tag{4.8c}$$

where α_F is the fine structure constant, L^3 is a normalization volume, $e_{+,-,z}$ and $e'_{+,-,z}$ are the components of the i-th polarization mode unit vector in the rotating coordinate ($e_{+,-} = e_x \pm ie_y, e_z = e_z$) in which the polarization matrix is diagonal. If there is no magnetic field, the cross section is entirely described by T_c. The magnetic field introduces the resonance features at $\omega \sim \omega_c$ which we find in the denominators of T_a and T_b and which strongly enhance the scattering probability of photons with energies corresponding to the ground Landau level. Summing all three terms, we get

$$\langle f \,|\, T \,|\, i\rangle = \frac{2\pi\alpha_F\hbar^2 c}{m\omega L^3}\Big(\frac{\omega}{\omega+\omega_c}e'^*_+e_+ + \frac{\omega}{\omega-\omega_c}e'^*_-e_- + e'^*_z e_z\Big). \tag{4.9}$$

We calculate the differential cross section from the scattering rate Q, which is the number of scattering per unit time, dividing it by the incoming flux c/L^3. Using Fermi's golden rule and the photon density $\rho = L^3\omega^2/(2\pi c)^3\hbar$ we obtain

$$Q = \frac{2\pi}{\hbar}|\,\langle f \,|\, T \,|\, i\rangle\,|^2\rho = \frac{\alpha_F^2\hbar^2}{m^2cL^3}\left|\frac{\omega}{\omega+\omega_c}e'^*_+e_+ + \frac{\omega}{\omega-\omega_c}e'^*_-e_- + e'^*_z e_z\right|^2 \tag{4.10}$$

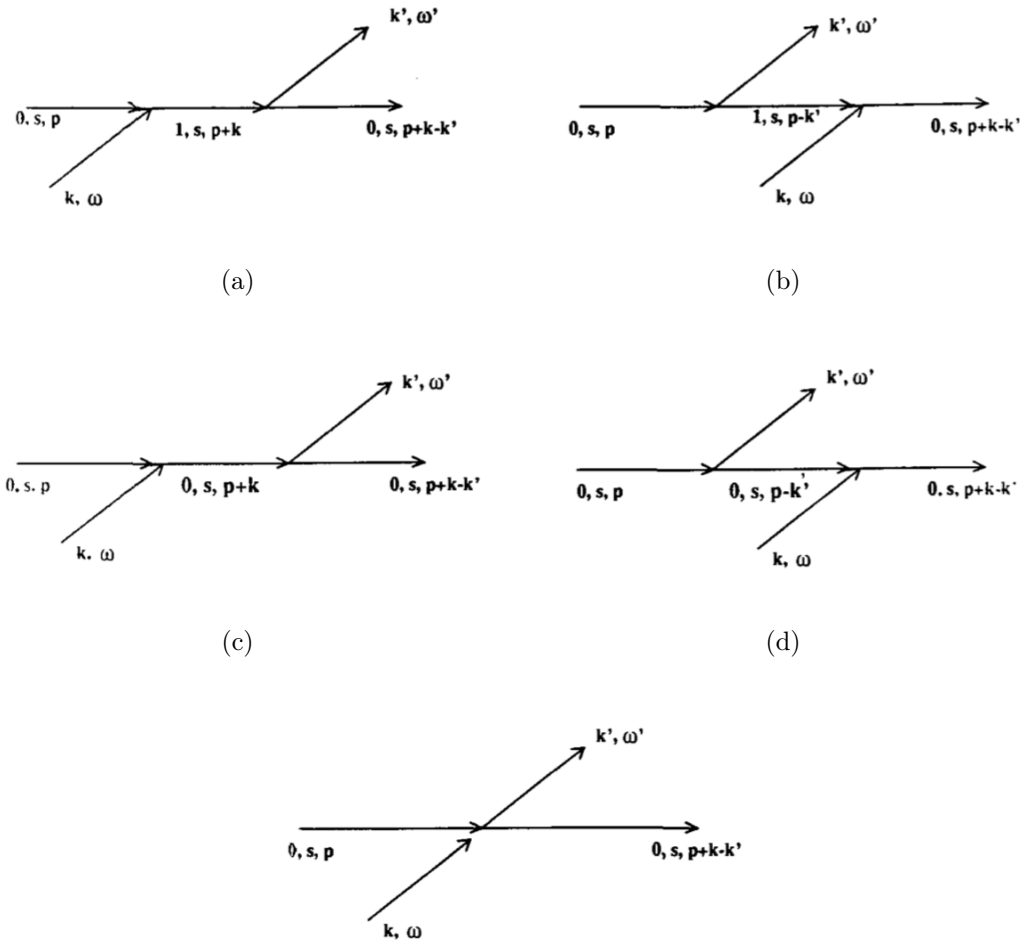

Figure 4.5: Feynman diagrams for Compton scattering in the case $n = n' = 0$ (Mészáros 1992).

and thus the differential cross section, calling $u = (\omega_c/\omega)^2$ is

$$\frac{d\sigma}{d\Omega}(\hat{e}', \hat{k}' \leftarrow \hat{e}, \hat{k}) = \alpha_F^2 \left(\frac{\hbar}{mc}\right)^2 \left| \frac{1}{1-u^{1/2}} e'^*_+ e_+ + \frac{1}{1-u^{1/2}} e'^*_- e_- + e'^*_z e_z \right|^2 . \tag{4.11}$$

In a hot plasma we cannot consider the electron at rest because thermal motions become important, so we have an electron momentum distribution $f(p)$ which we assume to be unidimesional along the magnetic field direction, taken to coincide with the z-axis; moreover we cannot use the dipole approximation. So now, there are 5 contributions to the scattering amplitude from the matrix $\langle f \,|\, T \,|\, i \rangle$ which correspond to the Feynman's diagrams in Figure 4.5 (setting

$\hbar = c = m = 1$):

$$T_a = \frac{2\pi\alpha_F}{\sqrt{\omega\omega'}L^3}\frac{\sqrt{\omega_c}\sqrt{\omega_c}}{\frac{1}{2}p^2+\omega-\omega_c-\frac{1}{2}(p+k)^2}e_-e'^*_- \tag{4.12a}$$

$$T_b = \frac{2\pi\alpha_F}{\sqrt{\omega\omega'}L^3}\frac{\sqrt{\omega_c}\sqrt{\omega_c}}{\frac{1}{2}p^2+\omega-\omega_c-\frac{1}{2}(p-k')^2-\omega-\omega'}e_+e'^*_+ \tag{4.12b}$$

$$T_c = \frac{2\pi\alpha_F}{\sqrt{\omega\omega'}L^3}\frac{(p+rk)(p+k-k'/2)}{\frac{1}{2}p^2+\omega-\frac{1}{2}(p+k)^2}e_ze'^*_z \tag{4.12c}$$

$$T_d = \frac{2\pi\alpha_F}{\sqrt{\omega\omega'}L^3}\frac{(p-k')(p-k'+k/2)}{\frac{1}{2}p^2+\omega-\frac{1}{2}(p-k')^2-\omega-\omega'}e_ze'^*_z \tag{4.12d}$$

$$T_e = \frac{2\pi\alpha_F}{\sqrt{\omega\omega'}L^3}(e'^*_+e_+ + e'^*_-e_- + e'^*_ze_z) \tag{4.12e}$$

where ω and ω' are the initial and final frequencies. Summing the 5 terms we obtain the scattering amplitude matrix

$$\langle f \mid T \mid i\rangle = \frac{2\pi\alpha_F\hbar^2c}{\sqrt{\omega\omega'}mL^3}(\Pi_+e'^*_+e_+ + \Pi_-e'^*_-e_- + \Pi_ze'^*_ze_z) \tag{4.13}$$

where Π is the polarization matrix whose components are ($\hbar = m = c = 1$)

$$\Pi_+ = 1 - \frac{\omega_c}{\omega'+\omega_c-pk'+k'^2/2} \tag{4.14a}$$

$$\Pi_- = 1 + \frac{\omega_c}{\omega-\omega_c-pk-k^2/2} \tag{4.14b}$$

$$\Pi_z = 1 + \frac{(p+k/2)(p+k-k'/2)}{\omega-pk-k^2/2} - \frac{(p-k'/2)(p-k'+k/2)}{\omega'-pk'+k'^2/2}\,. \tag{4.14c}$$

In order to obtain the differential cross section, we calculate the scattering rate Q_c as in the previous case, and we average it over the electron distribution function

$$Q_c = \frac{2\pi}{\hbar}|\langle f \mid \Pi \mid i\rangle|^2\delta(E_i - E_f) = \frac{\alpha_F^2\hbar^2\omega'}{m^2cL^3\omega}|\langle f \mid \Pi \mid i\rangle|^2\delta(\omega+\Delta\omega-\omega'). \tag{4.15}$$

The photon energy change is given by

$$\Delta\omega = \omega' - \omega = (p^2 - p'^2)/2\hbar m \tag{4.16}$$

and the momentum change is

$$\Delta p = p' - p = \hbar\Delta k = \frac{\hbar\omega'}{c}\cos\theta' - \frac{\hbar\omega}{c}\cos\theta \tag{4.17}$$

and so

$$\Delta\omega = \Delta k\frac{p}{m} - \hbar\frac{(\Delta k)^2}{2m}. \tag{4.18}$$

For given p, θ and θ', ω' is uniquely determined because energy and momentum must be conserved. So for a given initial and final state of the photon $(\omega, \theta, \omega', \theta')$ there is only one momentum for the electron

$$p_0 = m\frac{\Delta\omega}{\Delta k} + \frac{1}{2}\hbar\Delta k. \tag{4.19}$$

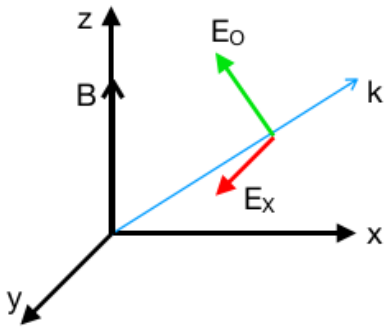

Figure 4.6: Reference frame used to calculate the polarization states.

It is easy now to average over p and we get the differential cross section

$$\frac{d^2\sigma}{d\omega' d\Omega'} = r_0^2 \frac{\omega'}{\omega} \frac{m}{|\Delta k|} f(p_0)(|\Pi_+ e'_+ e_+|^2 + |\Pi_- e'_- e_-|^2 + |\Pi_z e'_z e_z|^2). \tag{4.20}$$

As already said in chapter 2.2, in a strong magnetic fields radiation is nearly linearly polarized in two transverse modes, the O-mode and X-mode, which in the following we denote with 1 and 2 respectively. To calculate the polarization states, in the reference frame with $\boldsymbol{B}$ along the z-axis and the wave vector in the $x - z$ plane as in Figure 4.6, two orthogonal polarization state basis $|a\rangle$ and $|b\rangle$ are chosen

$$|a\rangle = \begin{pmatrix} -\cos\theta \\ 0 \\ \sin\theta \end{pmatrix}, \qquad |b\rangle = \begin{pmatrix} 0 \\ 1 \\ 0 \end{pmatrix} \tag{4.21}$$

We can evaluate the forward amplitude matrix elements

$$\langle a \,|\, T \,|\, a \rangle = \frac{1}{2} \cos^2\theta (T_+ - T_-) + \sin^2\theta \, T_z, \tag{4.22a}$$

$$\langle a \,|\, T \,|\, b \rangle = -\langle b \,|\, T \,|\, a \rangle = -\frac{i}{2} \cos\theta (T_+ - T_-), \tag{4.22b}$$

$$\langle b \,|\, T \,|\, b \rangle = \frac{1}{2}(T_+ - T_-) \tag{4.22c}$$

where $T_{+,-,z}$ are given by

$$T_{+,-,z} = \int dp f(p) \Pi'_{+,-,z}(p) \tag{4.23}$$

with Π'_i are the new polarization matrices which come from eq. 4.14 specialized to $\omega' = \omega$, $k' = k$ and adding the radiation damping $\gamma_r = 2e^2\omega^2/3mc^3$ so that the convergence of the integrals is ensured:

$$\begin{aligned} \Pi'_+ &= \frac{\omega - kp + k^2/2}{\omega + \omega_c - kp + k^2/2 + i\gamma_r} \\ \Pi'_- &= \frac{\omega - kp - k^2/2}{\omega - \omega_c - kp + k^2/2 + i\gamma_r} \\ \Pi'_z &= \frac{\omega}{k} \left(\frac{p + k/2}{\omega - kp - k^2/2 + i\gamma_r} - \frac{p - k/2}{\omega - kp + k^2/2 + i\gamma_r} \right) \end{aligned} \tag{4.24}$$

If we use a one-dimensional Maxwell-Boltzmann distribution for $f(p)$, we can rewrite the amplitude matrix elements using the plasma dispersion function $W(z)$(Fried & Conte 1961; Kirk 1980) which is convenient to use for numerical purposes

$$\begin{aligned} T_+^f &= 1 + i\sqrt{\pi}\frac{\omega_c + i\gamma_r}{\Delta\omega} W\left(\frac{\omega + \omega_c + k^2/2 + i\gamma_r}{\Delta\omega}\right) \\ T_-^f &= 1 - i\sqrt{\pi}\frac{\omega_c - i\gamma_r}{\Delta\omega} W\left(\frac{\omega - \omega_c - k^2/2 + i\gamma_r}{\Delta\omega}\right) \\ T_z^f &= -i\sqrt{\pi}\frac{\omega}{k}\frac{\omega + i\gamma_r}{\Delta\omega}\left[W\left(\frac{\omega - k^2/2 + i\gamma_r}{\Delta\omega}\right) - W\left(\frac{\omega + k^2/2 + i\gamma_r}{\Delta\omega}\right)\right] \end{aligned} \tag{4.25}$$

where $\Delta\omega = \omega \mid \cos\theta \mid (2kT/m)^{1/2}$. Diagonalizing the matrix T we obtain the polarization modes in the form

$$|e_1\rangle = \cos\psi\,|a\rangle + i\sin\psi\,|b\rangle\,, \qquad |e_2\rangle = -i\sin\psi\,|a\rangle + \cos\psi\,|b\rangle \tag{4.26}$$

with

$$\tan 2\psi = \frac{2i\,\langle a \mid T \mid b\rangle}{\langle a \mid T \mid a\rangle\,\langle b \mid T \mid b\rangle}. \tag{4.27}$$

In Figure 4.7 the differential scattering cross section is plotted for an incident ordinary photon of energy $\hbar\omega = 40$ keV and direction $\theta = 45°$ scattered into an extraordinary photon for four outgoing angles $\theta' = 20°, 70°, 120°, 160°$. As we can see, there are peaks in the cross section which corresponds to the cyclotron resonance, i.e. when $\omega = \omega_c$. The sharpness of this resonance is due to the fact that, giving θ and ω, just electrons with a particular velocity can absorb that photon, and giving θ', the ω' of the final electron is uniquely selected.

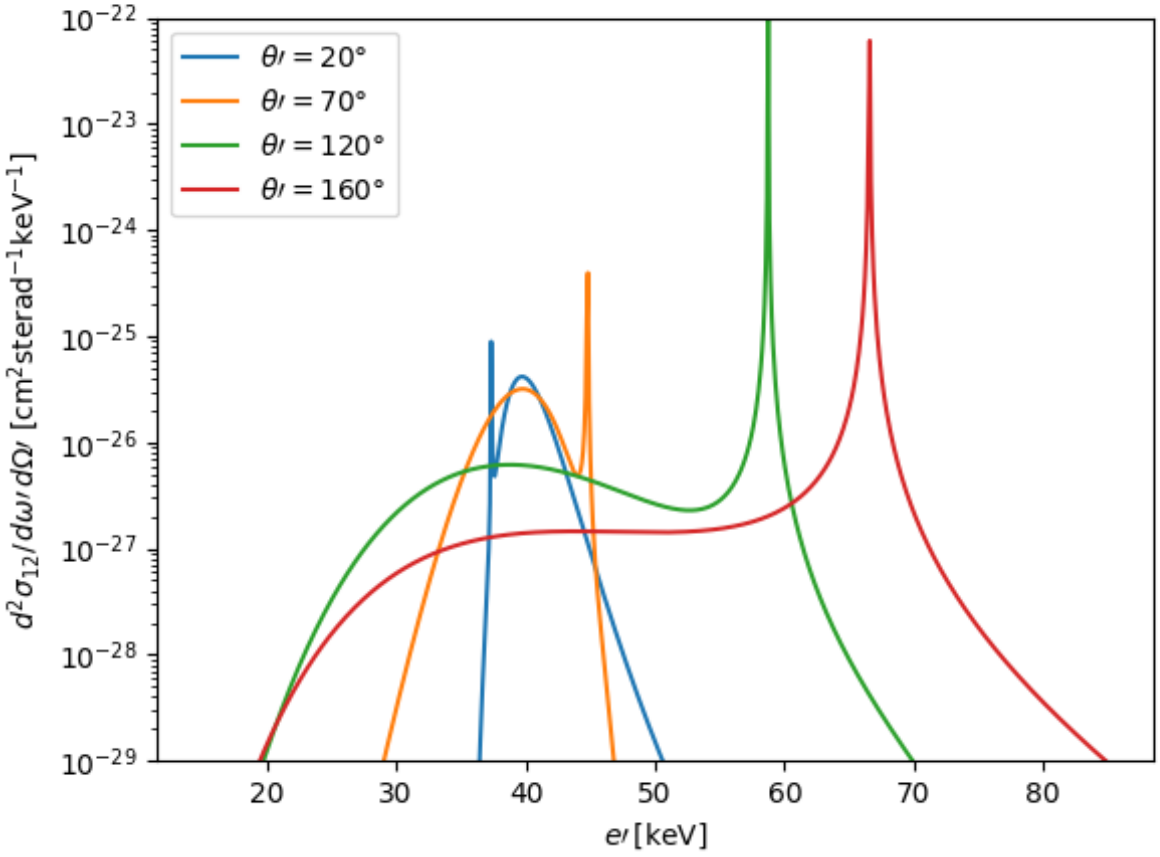

Figure 4.7: Differential scattering cross section $d^2\sigma_{12}/d\Omega' d\omega'$ for Compton scattering from ordinary (1) to extraordinary (2) photon as a function of the final photon energy computed for 4 different final angles $20°, 70°, 120°, 160°$. The incident photon has energy $\hbar\omega = 40$ keV and direction $\theta = 45°$, the plasma temperature is 10 keV and the cyclotron energy is 50 keV.

Chapter 5

Analysis of the cross section

The differential scattering cross section given by Nagel (1981) has been analyzed and integrated numerically (using the trapezoidal rule). The result is compared with the total cross section obtained through the optical theorem. First of all, we integrated eq. 4.20 over the outgoing photon energies (in the range $1 - 200$ keV) and angles (between 1° and 180°), for incoming photons in the energy range of $1 - 100$ keV. We initially assume an incoming photon angle of $\theta = 45^\circ$, a plasma temperature of 10 keV and a magnetic field of $\sim 10^{12}$ G as in the cited paper. In Figure 5.1 the total cross section for X-mode and O-mode photons is shown. The curves obtained through the numerical implementation fit very well the behavior predicted by the optical theorem

$$\sigma_{1,2} = -4\pi r_0 \frac{c}{\omega}\left(\mathrm{Im}\, T_+^f |e_+|^2 + \mathrm{Im}\, T_-^f |e_-|^2 + \mathrm{Im}\, T_z^f |e_z|^2\right). \tag{5.1}$$

As expected, the O-mode scattering cross section at low energies turns out to be of the order of the Thomson cross section, while the X-mode one increases as ε^2 in the same energy range (see equations 3.7). The oscillations around the resonance bump are due to two main reasons: firstly, the choice of the integration grid for, which we considered as uniform in the range $1 - 100$ keV and which is good for low energies, while it should be defined ad-hoc for higher energies and in particular in the range where the resonance appears; moreover the use of the trapezoidal rule for the integration is not that accurate.

However when we perform the same calculation for a just slightly higher temperature, the two curves start to diverge for low energies as we can see in Figure 5.2. For even higher temperatures this problem is even more significant. In Figure 5.3 we show the case of temperature of 50 keV.

To understand this behavior we have to consider the shape of the non-relativistic Maxwellian $f(p_c)$, which appears as a multiplicative factor in eq. 4.20 and introduces the dependence on the temperature in the differential cross section. If we focus on the momentum distribution function for a fixed incoming photon energy, we can see that an increase in the temperature produces a significant broadening (Figure 5.4).

This means that as the temperature increases the contribution of the scattering amplitudes at high outgoing photon energies becomes more and more important. Looking at the behavior

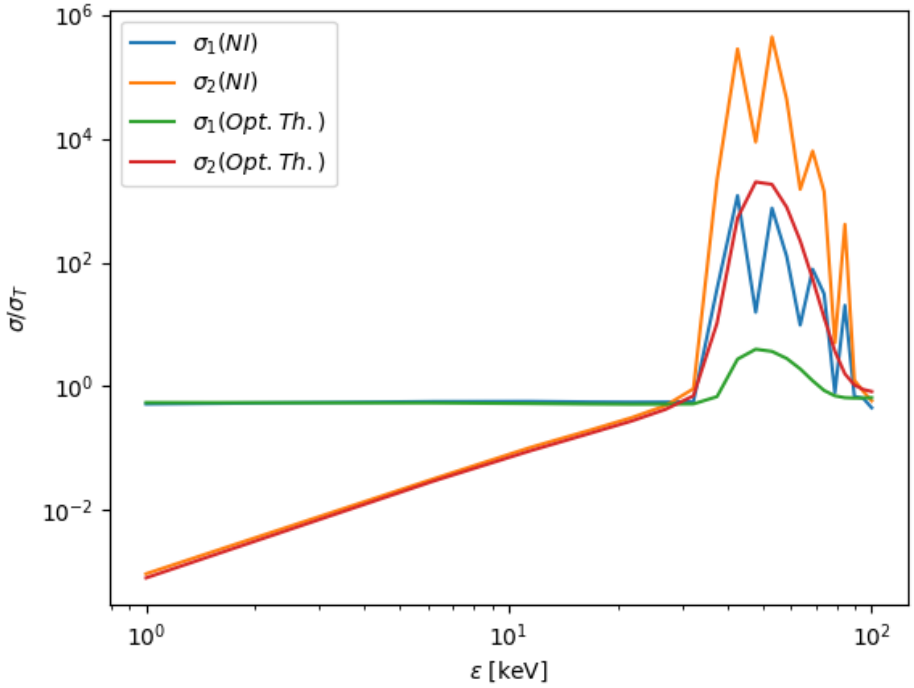

Figure 5.1: Total cross sections for the two modes normalized to the Thomson cross section. The subscripts 1 represent the ordinary mode while 2 the extraordinary mode. The red and green curves represent the total cross section calculated through optical theorem while the blue and yellow ones result from numerical integration.

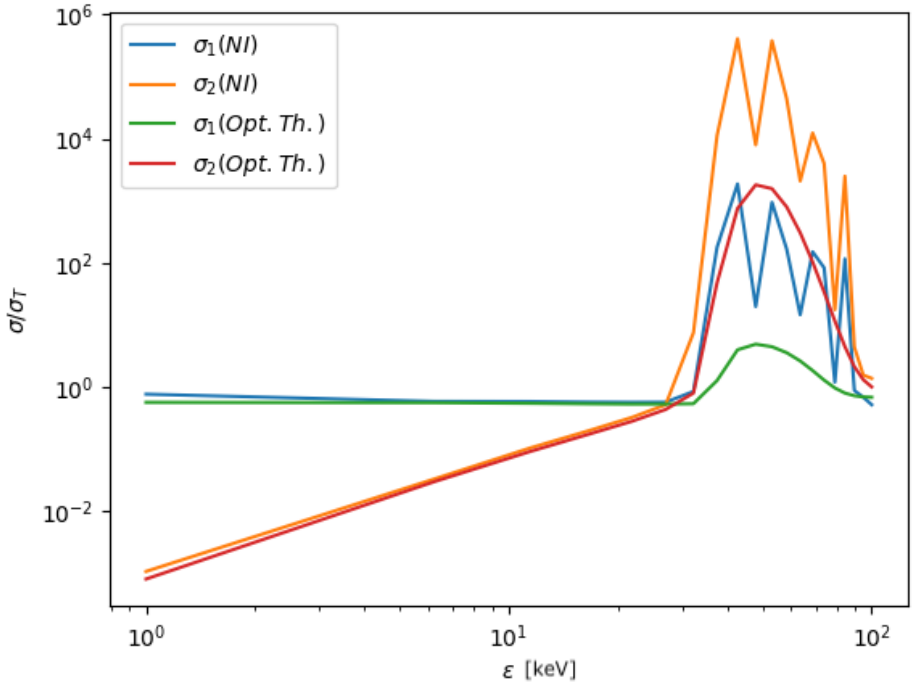

Figure 5.2: Total cross sections for the two modes as in Figure 5.1 but with $T = 14$ keV.

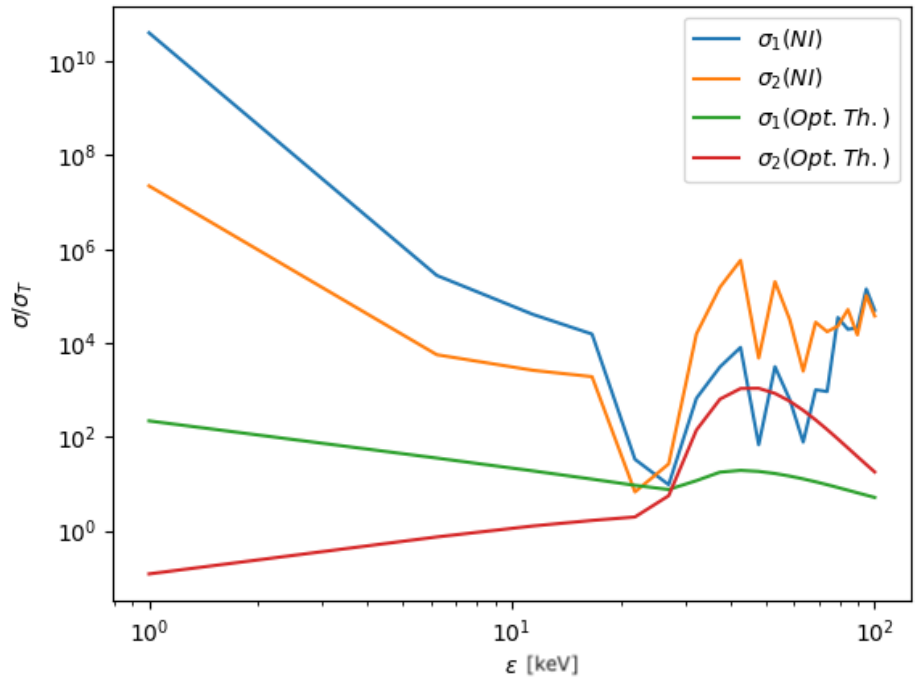

Figure 5.3: Total cross sections for the two modes as in Figure 5.1 but with $T = 50$ keV.

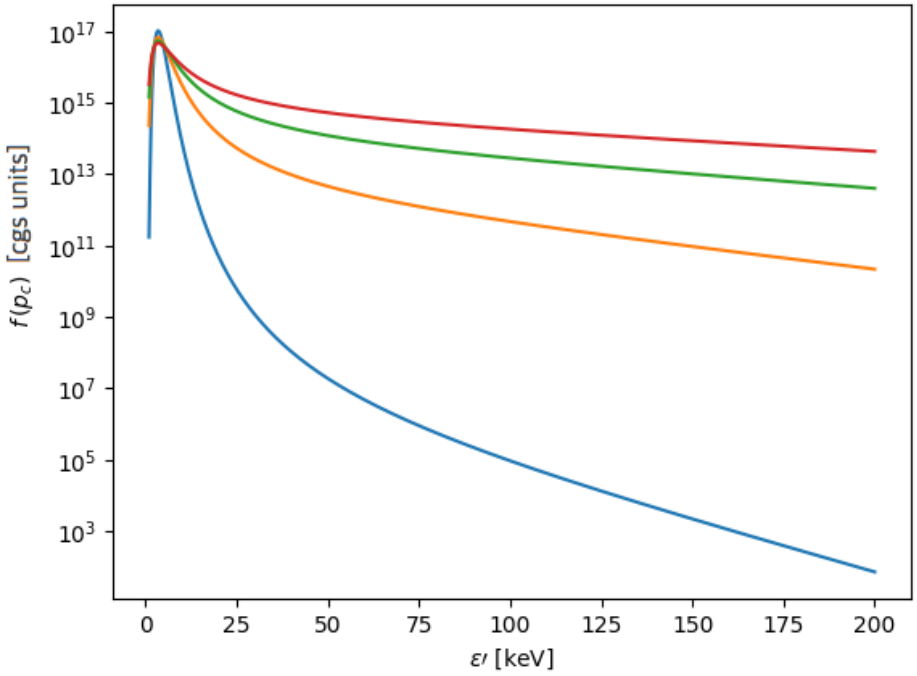

Figure 5.4: Momentum distribution function $f(p_c)$ for four values of the temperature in the case of an incoming photon with energy $\varepsilon = 3.5$ keV.

of the Π_+, Π_- and Π_z terms, for a low-energy incoming photon[1], we can easily see that the Π_+ and Π_- contributions are practically negligible over the almost entire ε' range, except for a clear divergence in correspondence of the cyclotron resonance (Figure 5.5a and 5.5b).

On the other hand, Π_z assumes much higher values and also shows a divergence at a higher energy than that of Π_+ and Π_- (Figure 5.6). In this way the Π_z term becomes predominant at higher ε', where $f(p_c)$ assumes higher values at higher temperatures. This causes the deviation at low incoming photon energies shown in Figure 5.3.

Contrary of Π_+ and Π_-, Π_z refers to the processes in which the virtual electron is in the Landau ground state, and so its divergence cannot be due to the resonance. Considering the denominator of the first fraction in Π_z (which refers to the scattering amplitude T_c), it turns out to be

$$-\hbar^2 k\Delta k^3 + (2m\hbar\omega - \hbar^2 k^2)\Delta k^2 - 2m\hbar\Delta\omega\Delta k\,, \tag{5.2}$$

that has three zeros. The first one is at $\Delta k = 0$, i.e.

$$\varepsilon' = \frac{\varepsilon\mu}{\mu'}\,. \tag{5.3}$$

Then, solving the remaining equation one has

$$-\frac{\varepsilon\mu\mu'^2}{\hbar c^3}\varepsilon'^2 + \frac{\varepsilon^2\mu^2\mu'}{\hbar c^3}\varepsilon' + \frac{2m\varepsilon\mu'}{\hbar c}\varepsilon' - \frac{2m\varepsilon\mu}{\hbar c}\varepsilon' = 0\,, \tag{5.4}$$

from which the second zero is clearly $\varepsilon' = 0$ while the third one turns out to be

$$\varepsilon' = \varepsilon\frac{\mu}{\mu'} + \frac{2mc^2}{\mu'}\left(\frac{\mu' - \mu}{\mu'\mu}\right). \tag{5.5}$$

The situation is the same for the second fraction (amplitude T_d) except for a minus sign in the third zero, which is in this case

$$\varepsilon' = \varepsilon\frac{\mu}{\mu'} - \frac{2mc^2}{\mu'}\left(\frac{\mu' - \mu}{\mu'\mu}\right). \tag{5.6}$$

Because of what we concluded above, we can say that the divergence of Π_z at high energies ε' should not be there. This is confirmed by Mushtukov et al. (2016), who derived the propagator associated to the amplitudes T_a, T_b, T_c and T_d. In their equation (35), it turns out that the denominator is of the form

$$V^2 - E_n^2\,, \tag{5.7}$$

where $V = \sqrt{m^2c^4 + p^2c^2} + \hbar\omega$ for a and c processes, $V = \sqrt{m^2c^4 + p^2c^2} - \hbar\omega$ for b and d processes and

$$E_n = \sqrt{m^2c^4 + p_v^2c^2 + 2\hbar nB/B_Q}\,, \tag{5.8}$$

with p_v the momentum of the virtual electron and n its Landau level. This denominator can be zero only in correspondence of the cyclotron resonance. However, since for c and d processes

[1] In fact, the deviations highlighted in Figure 5.2 and5.3 between the numerical integrated cross sections and those obtained through the optical theorem is larger at low incoming photon energies.

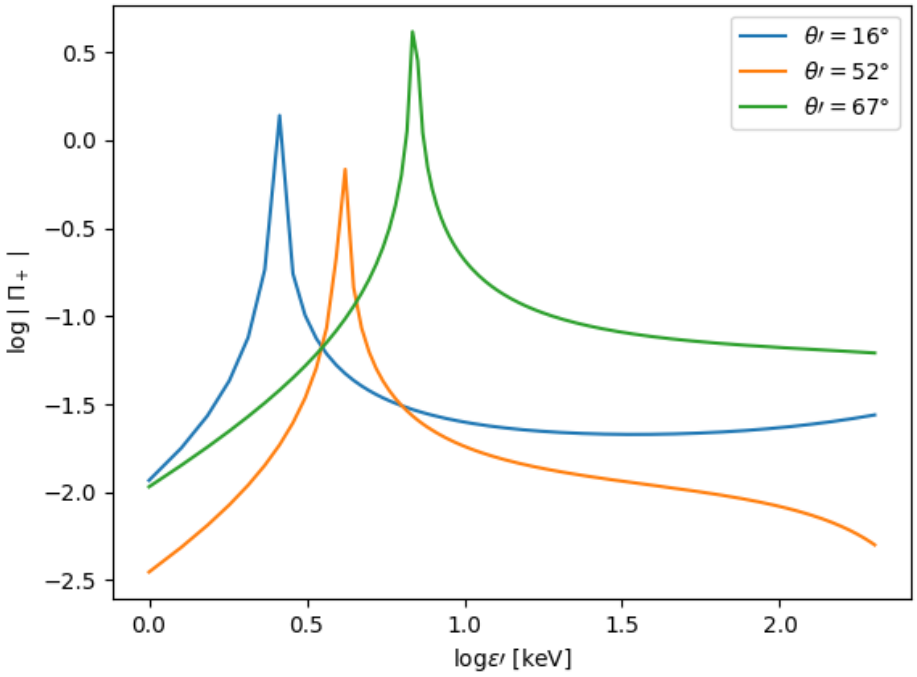

(a)

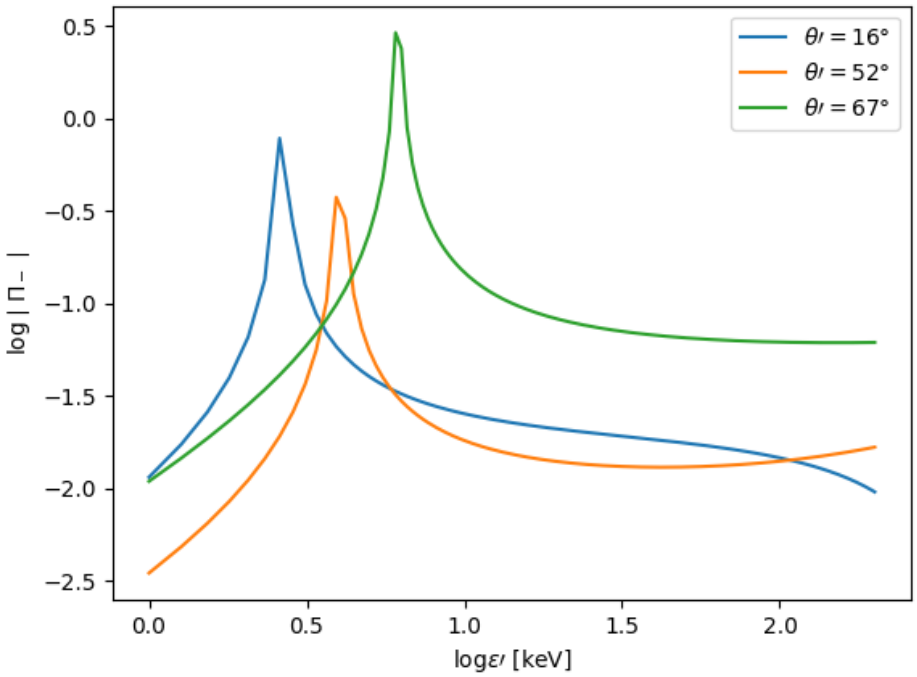

(b)

Figure 5.5: Polarization matrices Π_+ (a) and Π_- (b) for three outgoing angles $\theta' = 16°, 52°, 67°$, with $\varepsilon' = 3.5$ keV, $\theta = 45°$.

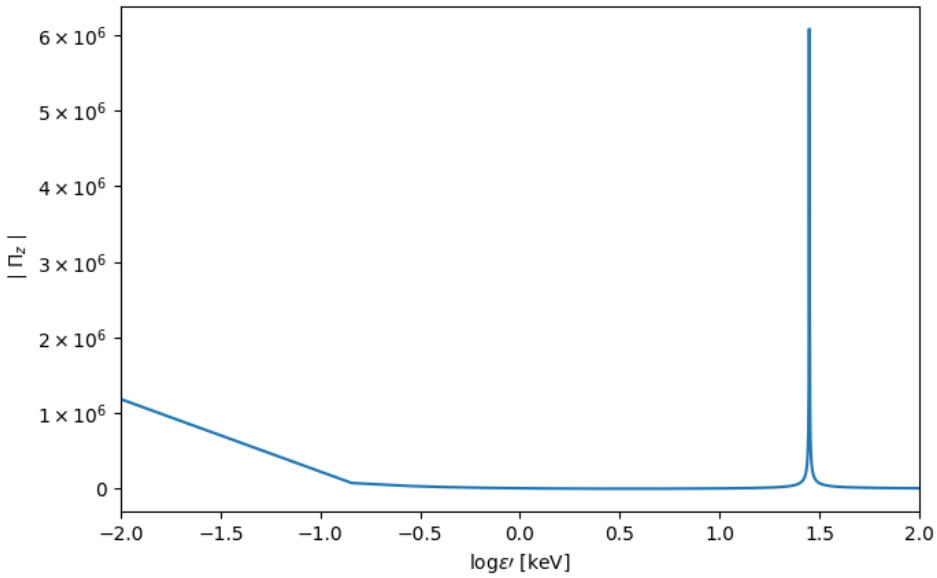

Figure 5.6: Polarization matrix Π_z for an outgoing angle $\theta' = 47°$, with $\varepsilon' = 3.5$ keV, $\theta = 45°$.

$n = 0$, the denominator becomes zero only for $\hbar\omega = 0$, which is unphysical, i.e. there are not divergences in the amplitude.

On the other hand, it can be noted that, using the non-relativistic approximation for the electron energy in V and E_n the denominator in equation (35) of Mushtukov et al. (2016) can be zero also at an energy

$$\hbar\omega = \frac{2mc^2}{\mu^2}\left(1 - \frac{p}{mc}\mu\right), \tag{5.9}$$

which is similar to the zero in the denominators of Π_z we found above. For this reason, we tried to calculate the Π_z term using the full relativistic energy for the electron. The result is shown in Figure 5.7: the divergence at high energy disappeared, but the width of the divergence at $\varepsilon' = 0$ is enhanced. This produces strong deviations in the total cross section with respect to that obtained via the optical theorem even at $T = 10$ keV which did not present this problem before.

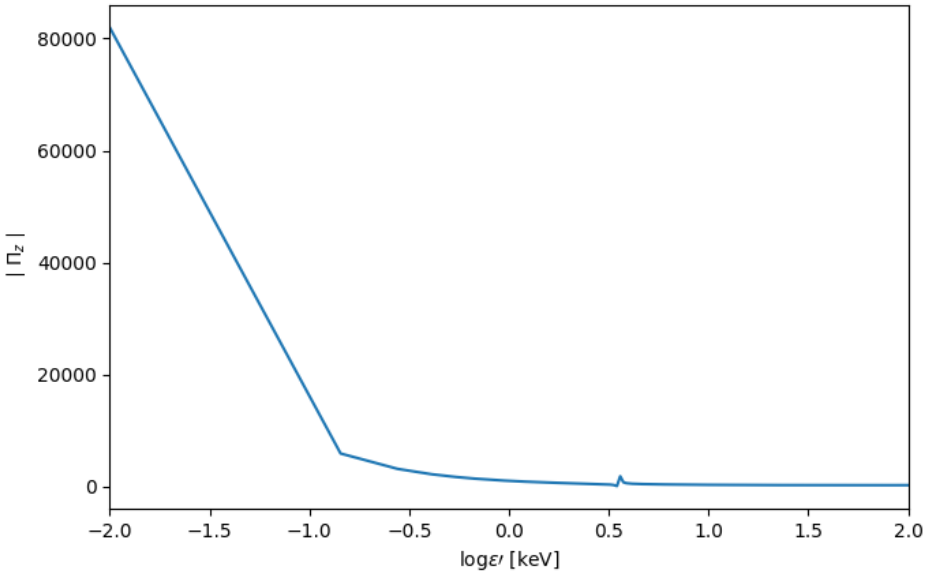

Figure 5.7: The scattering amplitude matrix Π_z calculated with the relativistic energy for the electrons and virtual electron.

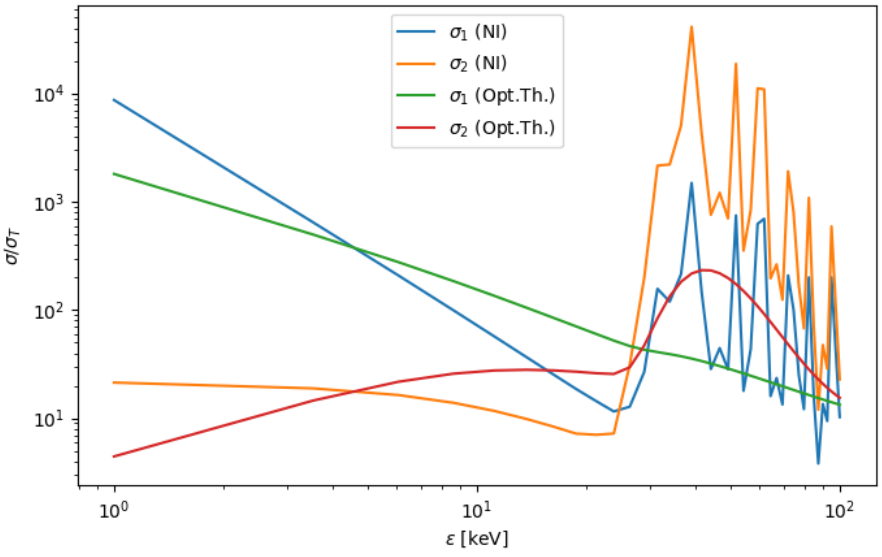

Figure 5.8: Total cross section for the two modes as in Figure 5.1 but with Π_z in the relativistic limit.

Chapter 6

Conclusion

The differential scattering cross section in a hot, strongly magnetized plasma has been analyzed in the non-relativistic limit. This process is crucial to describe the spectra of NSs which present the highest magnetic fields known in the universe. Moreover in structures like accretion columns in accreting pulsars, scattering is one of the largest source of opacity and it defines the emission pattern in the X-ray emission.

In the presence of a strong magnetic field, the motion of the charged particles is strongly anisotropic: they are free to move along the magnetic field direction while they are confined in quantized orbits perpendicularly to it. Moreover, photons are expected to be linearly polarized in the two normal modes, ordinary and extraordinary. The propagation of radiation in this magnetized medium depends on the polarization modes of photons which can change upon scattering. The scattering opacity for X-mode photons is strongly reduced with respect of O-mode photons by a factor $(\omega/\omega_c)^2$. Being ω_c proportional to the strength of the magnetic field, for high values of B the medium is optically thin for X-mode photons which can escape from the surface, while it remains optically thick for O-mode ones. Thus the radiation is expected to be linearly polarized mostly in the X-mode. Strong magnetic fields can also influence the propagation of photons in vacuo.

In order to solve the radiation transport equation, which has to be done separately for the two modes, and which allows to describe the observed spectra of these sources, a good treatment of the magnetic scattering process is needed for each combination of initial and final energies and angles. Although Thomson scattering has been studied deeply in literature, Compton scattering in strong magnetic fields still lacks of a formalism which allows to perform numerical simulations within reasonable computational times. In fact, the behavior of the magnetic scattering cross section is very complex and exhibits divergences for specific combinations of the incoming and outgoing photon directions and energies. Bringing under control these features, which were overlooked in past investigations, is extremely important in the numerical solution of the radiative transfer equation in a scattering-dominated medium beyond two-stream approximation.

Thus an analysis of the differential scattering cross section has been performed in the quantum formalism, analyzing the approach by Nagel (1981) and Mészáros (1992). This promises to

comply with the requirement of short computational times, since it provides analytical formulae for both the differential and total scattering cross sections. Nevertheless some problems arise: Nagel (1981) and Mészáros (1992) already noted that the occurrence of angular divergences forces to solve the problem in the two-stream approximation. Moreover, they showed the results for a temperature of 10 keV only.

We performed the same calculation just for a slightly higher temperature, we noticed that the cross section obtained through the numerical integration starts to diverge for low energies with respect to the one calculated with the optical theorem. At even higher temperatures, but still remaining in the domain of the non-relativistic limit, the two cross sections largely differ. To explain this behavior we analyzed the distribution function $f(p_c)$, which is the one that introduces the dependence on the temperature in the differential cross section. An increase in the temperature produces a significant broadening of this function which assumes higher values at high energies. This means that as the temperature increases the contribution of the scattering amplitudes at high outgoing photon energies becomes more and more important. We found that the contributions of the Π_+ and Π_- terms for a low-energy incoming photon are practically negligible over the almost entire ε' range while instead the Π_z term dominates at higher ε', where $f(p_c)$ assumes higher values at higher temperatures. We thus analyzed the Π_z amplitude and we tried to suppressed its divergency at high ε' which produces the deviation in the total scattering cross section at low incoming energies. We used the relativistic energy for the electrons to calculate the scattering propagate since, as shown by Mushtukov et al. (2016), in the relativistic formalism the divergence does not appear. In this way the divergence at high energy disappears instead the one at $\varepsilon' = 0$ is strongly enhanced. This produces again an overestimate of the total cross section even at $T = 10$ keV and which makes this approach useless.

More tests are currently underway to describe the magnetic scattering cross section.

Bibliography

[1] Adler S. L., 1971, Ann. Phys., 67, 599

[2] Baade W., Zwicky F., 1934, Proc. Nat. Acad. Sci., 20, 254

[3] Basko M. M., Sunyaev R. A., 1975, A&A, 42, 311

[4] Basko M. M., Sunyaev R. A. 1976, MNRAS, 175, 395

[5] Becker A. P., Wolff M. T., 2007, ApJ, 654, 435

[6] Burke-Spolaor S., Bailes M., 2010, Astron. Soc., 855, 866

[7] Caballero I., Wilms J., 2012, MmSAI, 83, 230

[8] Camenzind M., 2007, Compact objects in astrophysics: white dwarfs, neutron stars, and black holes. Astronomy and astrophysics library, Berlin, Springer-Verlag,

[9] Canuto, V., Lodenquai, J., Ruderman, M. 1971, Phys. Rev. D, 3, 2303

[10] Duncan R. C., Thompson C., 1992, ApJ, 392, L9

[11] Fried B. D., Conte S. D., 1961, The Plasma Dispersion Function. London: Academic Press

[12] Gnedin Yu. N., Pavlov G. G., 1974, Soviet Phys.-JETP Lett., 38, 903

[13] Halpern J. P., Gotthelf E. V., 2010, ApJ, 709, 436

[14] Harding A. K., Lai D., 2006, Rep. Prog. Phys., 69, 2631

[15] Hewish A., Bell S. J., Pilkington J. D. H., Scott P. F., Collins R. A., 1968, Nature, 217, 709

[16] Heyl J. S., Shaviv N. J., 2002, Phys. Rev. D, 66, 023002

[17] Heyl J. S., Shaviv N. J., Lloyd D., 2003, MNRAS, 342, 134

[18] Ho W. C. G., Lai D., 2003, MNRAS, 338, 233

[19] Kirk J., 1980, Plasma Phys., 22, 639

[20] Lorimer D., Kramer M., 2005, Book Review: Handbook of Pulsar Astronomy. Cambridge University Press, The Observatory

[21] Lyne A. G., McLaughlin M. A., Keane E. F., Kramer M., Espinoza C. M., Stappers B. W., Palliyaguru N. T., Miller J., 2009, 400, 1439

[22] McLaughlin, M. A., Lyne, A. G., Lorimer, D. R., et al. 2006, Nature, 439, 817

[23] Mészáros P., 1992, High-Energy Radiation from Magnetized Neutron Stars. University of Chicago Press, Chicago, IL

[24] Mészáros P., Ventura J., 1979, Phys. Rev. D., 19, 3565

[25] Mignani R. P. et al., 2008, A&A, 488, 267

[26] Mushtukov A. A., Nagirner D. I., Poutanen J., 2016, preprint (arXiv:1512.06681v2)

[27] Nagel W., 1981, ApJ, 251, 288

[28] Nelson R. W., Salpeter E. E., Wasserman I., 1993, ApJ, 418, 874

[29] Pavlov G. G., Gnedin Y. N., 1984, ASPR, 3, 197

[30] Potekhin A. Y., Chabrier G., 2003, ApJ, 585, 955

[31] Potekhin A. Y., Lai D., Chabrier G., Ho W. C. G., 2004, ApJ, 612, 1034

[32] Poutanen J., Mushtukov A. A., Suleimanov V. F., Tsygankov S. S., Nagirner D. I., Doroshenko V., Lutovinov A. A., 2013, ApJ, 777, 115

[33] Soffitta P. et al., 2013, Nucl. Instrum. Methods Phys. Res. A, 700, 99

[34] Taverna R., Turolla R., 2017, MNRAS, 469, 3610

[35] Taverna R., Turolla R., Gonzalez Caniulef D., Zane S., Muleri F., Soffitta P., 2015, MNRAS, 454, 3254